Improving Parameterization of Combustion Processes in Coupled Fire-Atmosphere Models through Infrared Remote Sensing

Final Report for Project Number RC-2643

PI: Scott L. Goodrick, USDA Forest Service

Co-PIs: Joseph J. O'Brien, USDA Forest Service

E. Louise Loudermilk, USDA Forest Service
Rodman R. Linn, Los Alamos National Laboratory

Collaborators: Ginny A. Marshall, Canadian Forest Service

REPORT DOCUMENTATION PAGE

Form Approved
OMB No. 0704-0188

1. REPORT DATE *(DD-MM-YYYY)*	**2. REPORT TYPE**	**3. DATES COVERED** *(From - To)*
31/12/2022	SERDP Final Report	

4. TITLE AND SUBTITLE

Improving Parameterization of Combustion Processes in Coupled Fire-Atmosphere Models through Infrared Remote Sensing

5a. CONTRACT NUMBER

5b. GRANT NUMBER

5c. PROGRAM ELEMENT NUMBER

6. AUTHOR(S)

Scott L. Goodrick, Joseph J. O'Brien and E. Louise Loudermilk
USDA Forest Service

Rodman Linn
Los Alamos National Laboratory

Ginny Marshall
Canadian Forest Service

5d. PROJECT NUMBER
RC-2643

5e. TASK NUMBER

5f. WORK UNIT NUMBER

7. PERFORMING ORGANIZATION NAME(S) AND ADDRESS(ES)
USFS Southern Research Station
320 Green St.
Athens, GA 30602

8. PERFORMING ORGANIZATION REPORT NUMBER
RC-2643

9. SPONSORING/MONITORING AGENCY NAME(S) AND ADDRESS(ES)
Office of the Deputy Assistant Secretary of Defense (Energy Resilience & Optimization)
3500 Defense Pentagon, RM 5C646
Washington, DC 20301-3500

10. SPONSOR/MONITOR'S ACRONYM(S)
SERDP

11. SPONSOR/MONITOR'S REPORT NUMBER(S)
RC-2643

12. DISTRIBUTION/AVAILABILITY STATEMENT

DISTRIBUTION STATEMENT A. Approved for public release: distribution unlimited.

13. SUPPLEMENTARY NOTES

14. ABSTRACT

The overall goal of this project was to improve the representation of combustion processes in coupled fire-atmosphere models operating at the landscape level. Models intended to be used for landscape-scale fires (hundreds of meters to 10s of kilometers), typically divide the simulation domain up into a mesh of grid cells and these grid cells typically range in size from 1-30 meters on a side. As the processes governing combustion occur on considerably smaller scales, models require a means of describing these processes capable of dealing with heterogeneity within a cell and must also be scalable if the cell size is changed. A detailed examination of these combustion processes will improve our understanding of fine-fuel heat exchange, ignition, and fire spread and how fire behavior may be affected by fuel conditions. The specific objectives of the project are to: 1) Track real-time high-resolution fuel moisture dynamics and fuel consumption at sub-meter scale in natural fuel beds containing both live and dead fuels; 2) Evaluate the subgrid-scale parameterization of solid-phase combustion used in a coupled fire-atmosphere models; 3) Examine how model resolution affects the level of detail required in subgrid scale models of combustion processes; 4) Examine interactions among fuel heterogeneity, in both arrangement and load that influences fire spread, principally through fire-atmosphere interactions.

15. SUBJECT TERMS

Combustion, parameterization, modelling, wildland fire, fire behavior

16. SECURITY CLASSIFICATION OF:			**17. LIMITATION OF ABSTRACT**	**18. NUMBER OF PAGES**	**19a. NAME OF RESPONSIBLE PERSON**
a. REPORT	**b. ABSTRACT**	**c. THIS PAGE**			Scott Goodrick
UNCLASS	UNCLASS	UNCLASS	UNCLASS	70	**19b. TELEPHONE NUMBER** *(Include area code)* 706-559-4237

Table of Contents

Keywords

Combustion, parameterization, modelling, wildland fire, fire behavior

List of Tables

List of Figures

Temperature is plotted only when the respective fuel density is above $1x10^{-6}$ kg m^{-3} and shading indicates 1 standard deviation above and below the mean temperatures.

14 Results for wind speed and moisture fractions applied to the low-intensity gas scenario. 51

15 Individual term contributions averaged over 1 s for a) the dry fuel temperature equation, b) the dry fuel variance equation, c) the wet fuel temperature equation and d) the wet fuel variance equation in the wind 2 m s^{-1}, fuel moisture fraction 2 and gas temperature 500 K scenario. The terms in the legend appear as ordered in the derived equations and are discussed further in Table 3. All terms shown are multiplied by $\frac{\Delta t}{c_p \rho}$ or $\frac{2\Delta t}{c_p \rho}$ for the corresponding specific heat capacity and density. 54

16 Wind speed and fuel density scenarios for gas temperature oscillating between 1200 K and 300 K with a 60 s period. The wind and moisture scenarios are the same as described in Figure 13. 56

17 Comparison of the effects for different gas temperature variances on the dry fuel variance for a) 0.1 m s^{-1}, b) 1.0 m s^{-1} and c) 2.0 m s^{-1} winds. In all simulations the mean gas temperature is 500 K, the moisture fraction is 1 and ϕ_{gx} is a measure of the gas temperature variance, with x corresponding to half the maximum width of the top hat. 59

18 Simulation results for the mean wet solid fuel, dry fuel and gas temperatures (blue, red, grey solid lines) compared with observations (dashed lines) of mean solid temperature evolution in a 1 m x 1 m cell. The horizontal line is at 773 K (500 C) which is the minimum observed FLIR temperature. The adjusted dry fuel temperature (thick solid black line) is the recalculated mean temperature for temperatures above 773 K. 61

19 Simulation results for modeled variance (solid line) compared with observations of variance in a 1 m x 1 m cell. The adjusted variance is recalculated after removing all temperatures below 773 K, as discussed in Figure 18. 62

List of Acronyms

CFD	Computational Fluid Dynamics
FRFD	Fire Radiated Flux Density
IR	Infrared
NDVI	Normalized Difference Vegetation Index
PDF	Probability Distribution Function
PIV	Particle Image Velocimetry

Abstract

Objectives: The overall goal of this project was to improve the representation of combustion processes in coupled fire-atmosphere models operating at the landscape level. Models intended to be used for landscape-scale fires (hundreds of meters to 10s of kilometers), typically divide the simulation domain up into a mesh of grid cells and these grid cells typically range in size from 1-30 meters on a side. As the processes governing combustion occur on considerably smaller scales, models require a means of describing these processes capable of dealing with heterogeneity within a cell and must also be scalable if the cell size is changed. A detailed examination of these combustion processes will improve our understanding of fine-fuel heat exchange, ignition, and fire spread and how fire behavior may be affected by fuel conditions. The specific objectives of the project are to: 1) Track real-time high-resolution fuel moisture dynamics and fuel consumption at sub-meter scale in natural fuel beds containing both live and dead fuels; 2) Evaluate the subgrid-scale parameterization of solid-phase combustion used in a coupled fire-atmosphere models; 3) Examine how model resolution affects the level of detail required in subgrid scale models of combustion processes; 4) Examine interactions among fuel heterogeneity, in both arrangement and load that influences fire spread, principally through fire-atmosphere interactions.

Technical Approach: This project consists of a combination of field experiments and model simulations. The field experiments focus on intensive measurements of small 4 by 4 meter blocks. Fuel moisture and consumption measurements will utilize remote sensing techniques. For fuel moisture, we use a combination of infrared remote sensing and targets of known radiative properties to solve a system of equations that yield estimates of moisture fluxes from the vegetation. Additional infrared remote sensing techniques developed in the laboratory to estimate fire radiative power and fuel consumption are used for measuring natural fuels in the field. These two techniques combined track sub-meter scale changes in fuel moisture and consumption. Estimates of sensible heat flux are obtained from flow field estimates obtained through image analysis of visible imagery. Probability density functions are often used to represent subgrid variability, which is not typically known in detail from the field or explicitly resolved due to computational constraints. Such subgrid models have long been acknowledged as a key to model versatility and their refinement is critical to allow the use of these models in a wider range of scenarios and fire scales. Based on the measurements obtained in the field portion of this study, a new parameterization for sub-grid processes related to temperature and moisture variation in wildfire behavior models has been developed. The aim of the work described here is to improve the overall performance of these models, particularly during lower-intensity fires where the sub-grid spatial and temporal variations have significant impacts on fire behavior.

Benefits: The majority of fire model validation studies focus on comparing simulated fire perimeters to what was observed. While this may serve as a first cut at validation, it raises the question of whether the model is getting the right answer for the right reason. Only by looking at the small-scale processes can we gain confidence in the model. This study examined fuel moisture and temperature dynamics at the sub-meter scale to facilitate improved representations of combustion in fire spread models operating at the landscape scale. This project will benefit Department of Defense managers by improving our understanding of fuel moisture and temperature dynamics and advancing the capabilities of coupled fire-atmosphere models through improved subgrid parameterizations that will improve model performance in conditions consistent with a wide range of prescribed fire applications.

Executive Summary

Introduction

Wildfire behavior and spread are influenced by complex processes involving interactions between the fire and its surroundings. These interactions depend heavily on dynamic and heterogeneous turbulent flow fields that connect the fire to the fire environment, surrounding atmosphere, fuels, and topography. Computational fluid dynamic (CFD) techniques are used in physics-based fire behavior models to represent the coupled fire-atmosphere interaction using partial differential equations. These formulations describe the exchange of mass, momentum, and energy through non-linear processes such as convective and radiative heating and cooling, drag, turbulence, combustion, and evaporation. However, since wildland fires occur at large spatial scales and involve complex non-linear processes occurring at a wide variety of scales, it is not feasible to resolve all important phenomena over all relevant scales. Thus, sub-models or parameterizations must be developed to capture the net effects of these sub-grid phenomena.

Recent CFD-based wildfire studies have focused on understanding the behavior of intense wildfire scenarios, which are the most challenging to manage and pose significant risks to people, communities, and infrastructure. The characteristic length scales of dominant fire phenomena and fire geometry typically increase with the intensity of the fire, while the sensitivity of fires to fine-scale variations in the ambient environment and the significance of fine-scale variations in fire conditions decrease with the increase in the characteristic length scales. When conditions are extreme and fires are intense, existing physics-based wildfire behavior models typically perform well. However, the spatial scales of fire behavior are smaller and the importance of finer scale variations in fire activity and fire environment is greater during lower-intensity fires. As the relevant length scales of the fire decrease relative to feasible model resolution, many physical wildfire behavior models struggle in this regime.

Physics-based coupled fire atmosphere models use a series of coupled partial differential equations to track the evolution of mass, momentum, energy, turbulence, and species of the gases moving around a fire and the mass, moisture content, and temperature of the fuel. These models are typically solved numerically on a three-dimensional grid, and the temperature and moisture variations that govern some ignition and drying processes can be explicitly resolved on meter scales. However, even at the sub-meter scale, there can be distributions of temperatures and moisture conditions. Currently, these models employ the notion of a probability distribution function (PDF) of temperatures within each grid cell to determine the moisture evaporation and combustion rates. Using this approach, they avoid having a step function in the rate of evaporation or combustion associated with the mean temperatures reaching critical values. However, the current formulation still presents challenges for low-intensity fire scenarios, where the moisture and temperature heterogeneity scales are even more poorly resolved. As the importance of fine-scale variations increases with decreasing physical scales of the fires, the need for a more dynamic and scenario-dependent representation of sub-grid distributions becomes more apparent.

The overall goal of this project is to improve the representation of subgrid-scale processes in coupled fire-atmosphere models operating at the landscape level through the use of fine-scale infrared remote sensing at the plot level. Infrared remote sensing, along with some additional measurements of the ambient environment, allows us to track the temporal evolution of fuel temperature and fuel moisture flux in heterogeneous fuel beds at a sub-meter scale, ideal for evaluating subgrid scale combustion processes in the coupled model. The measurements need to be amenable to similar averaging, as the governing equations for these models describe changes in model variables averaged over a grid volume.

The current FIRETEC formulation explicitly tracks a mean solid fuel temperature and allows an assumed temperature variance. The combination is used to determine how much of the fuel is hot enough to evaporate water and to begin combusting as the temperature of the mean fuel increases. However, this approach suffers when conditions are less extreme and the length scales are small. In such cases, a parameterization needs to be flexible to account for multiple physical processes occurring at a given cell temperature based on variations in the environment. The aim of the work described here is to improve the overall performance of models like FIRETEC, particularly during lower-intensity fires where the sub-grid spatial and temporal variations have significant impacts on fire behavior.

Objectives

The overall goal of this project is to improve the representation of combustion processes in coupled fire-atmosphere models operating at the landscape level. Models intended to be used for landscape-scale fires (hundreds of meters to 10s of kilometers), typically divide the simulation domain up into a mesh of grid cells and these grid cells typically range in size from 1-30 meters on a side. As the processes governing combustion occur on considerably smaller scales, models require a means of describing these processes that is capable of dealing with heterogeneity within a cell and must also be scalable if the cell size is changed. A detailed examination of these combustion processes will improve our understanding of fine-fuel heat exchange, ignition, and fire spread and how fire behavior may be affected by fuel conditions. The specific objectives of the project are to:

- Track real-time high-resolution fuel moisture dynamics and fuel consumption at sub-meter scale in natural fuel beds containing both live and dead fuels.
- Evaluate the subgrid-scale parameterization of solid-phase combustion used in coupled fire-atmosphere models
- Examine how model resolution affects the level of detail required in subgrid-scale models of combustion processes.
- Examine interactions among fuel heterogeneity, in both arrangement and load that influences fire spread, principally through fire-atmosphere interactions.

- Use knowledge gained in pursuit of the first four objectives to advance a new parameterization for fuel consumption in FIRETEC that is better capable of responding to fine-scale variation in the fire environment.

Technical Approach

The focus of this study is to improve our understanding of how subgrid processes influence the combustion process in FIRETEC. In each burning cell, the local rate of combustion is described in terms of the change in bulk density of fine fuel particles with time which is a function of the local bulk densities of fuel and oxygen, turbulent mixing, along with the fraction of the computational cell that is actively burning. Currently, in FIRETEC, the burning fraction of the computational cell is defined as a probability distribution function (PDF) that determines the fraction based on the temperature of the cell, and this fraction is used to determine both the moisture evaporation and combustion rates for the cell. Assessing how well this PDF performs requires fine-scale estimates of temperature to be able to estimate a measured analog to the model's PDF. Additionally, to guide any refinement of the parameterization, we also obtain additional fine-scale measurements to help us understand the system. These additional measurements include estimates of the reaction rate, fluxes of moisture, and flow field measurements to provide estimates of the turbulent mixing term in the reaction rate. Understanding these fine-scale processes will guide improvements to the parameterization of the reaction rate.

Measurements for this study are collected using both infrared and visual cameras mounted on tall tripods within the burn units. The height of the nadir-view tripod system (8.2m) provided a 4.8x6.4m field of view for the infrared camera with a pixel size on the order of a square centimeter, providing sufficient resolution to allow scaling of quantities to the square meter and larger sizes to represent model cell sizes. The infrared camera is used to directly estimate the fraction of a model grid cell equivalent area burning, as well as provide additional estimates of fuel consumption and fuel drying to aid in assessing the relative role of different subgrid processes. For estimating the fractional area burning, the fraction of pixels above the Draper point (525°C) within an analysis block was used. The size of analysis blocks was varied from 1 cm^2 up to 4 m^2 to assess possible model resolution influences on subgrid phenomena.

It has been demonstrated that fire radiative energy is linearly related to the total amount of fuel consumed, and that fire radiative power is linearly related to the rate of fuel consumption in a statistically significant manner (Wooster, 2002; Wooster et al., 2005). Freeborn et al (2008) utilized infrared remote sensing in a laboratory setting to evaluate relationships between energy release, fuel mass loss, and emissions with good success. Loudermilk et al (2012) employed infrared thermography to explore links between fuel structure and fire behavior at fine scales in natural fuel beds. As expected, a linear relationship was found between energy release and fuel consumption

To assess fuel drying with infrared imagery, a new methodology was developed based on solving a coupled set of surface energy budgets for the fuel and a set of targets of known radiative

properties inserted in the fuel bed. The targets streamline the calculation process by removing the need for additional measurements such as a pyranometer for estimating solar radiation and fine-scale estimates of the flow field. The targets are designed to have similar aerodynamic properties as the vegetation but each target has a different known albedo. Since the targets lack moisture, their energy budgets lack the latent heat flux term, and the aerodynamic similarity results in a system of three equations with three unknowns: incoming solar radiation, sensible heat flux, and latent heat flux for the fuels.

Information on fine-scale fire-induced flows is obtained using visual imagery and applying cross-correlation particle image velocimetry (PIV). As an unseeded PIV measurement technique, we relied on patterns generated by the fire: flames, smoke, and ash particles as our unseeded tracers. These fine-scale flow fields are used to improve our understanding of subgrid turbulence being produced by subgrid combustion and how this turbulence can sustain the combustion process in the absence of turbulent mixing driven by larger-scale motions.

Our goal with these measurements was to develop and demonstrate techniques for collecting sub-meter scale measurements suitable for investigating the subgrid parameterization of a range of physical processes within a coupled fire-atmosphere model such as FIRETEC. While our focus in this study is the parameterization of the combustion process and specifically the form of a PDF used in that parameterization, our measurements extended beyond what was needed to investigate that specific parameterization by including estimates of moisture fluxes and turbulent flow dynamics to foster a more holistic understanding of subgrid processes that will lead to further investigations.

Results and Discussion

Using the Draper point as the transition point between burning and not burning, the pixels of each infrared image can be transformed into a binary image of pixels burning or not burning. Various size averaging windows can then be applied to both images to determine the mean temperature within the averaging window and the fraction of pixels within that window that are burning (Figure ES-1).

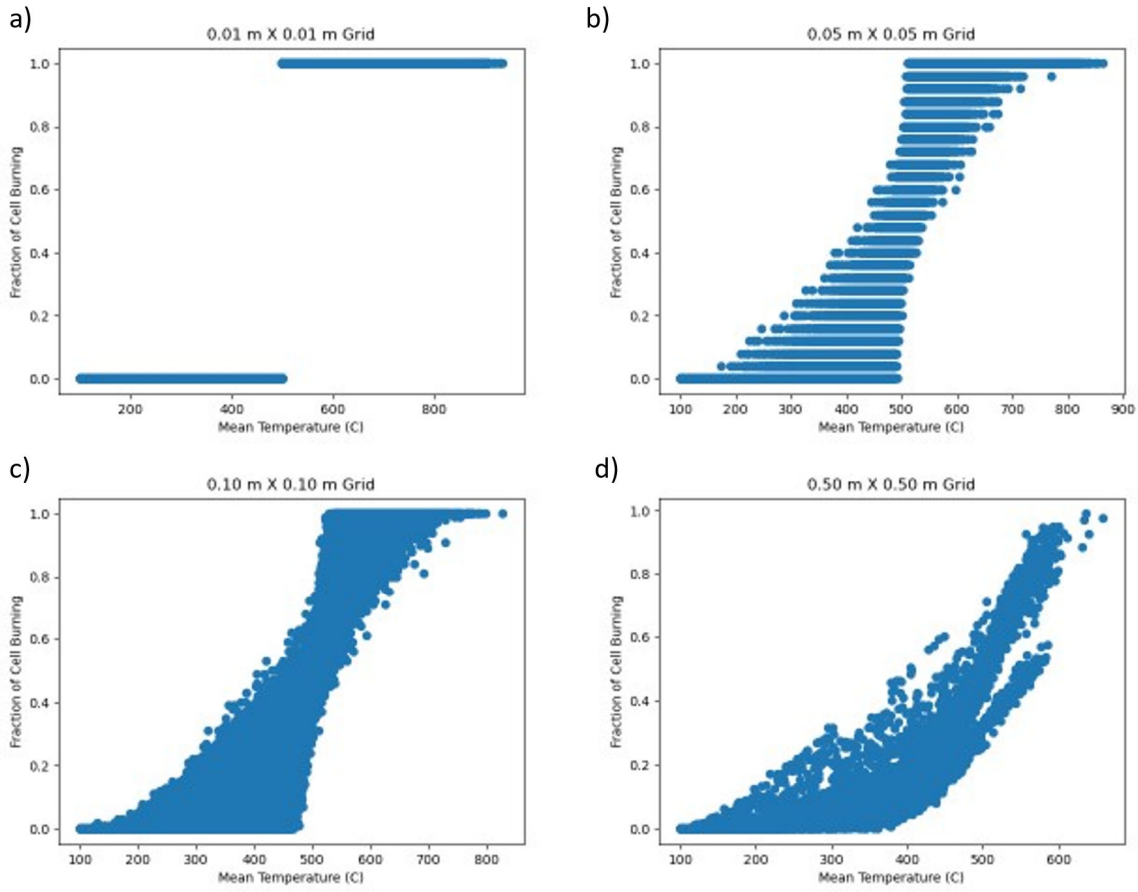

Figure ES-1. Fraction of computational cell burning as a function of mean temperature derived from FLIR imagery for grid sizes of a) 0.01m, b) 0.05m, c) 0.10m, and d) 0.50m.

The finest scale used in Figure ES-1a is at the pixel resolution of the camera which yields a step function as cells are either burning or not, but increasing the resolution by a factor of 5 (Figure ES-1b) yields a broad range of mean temperatures that can correspond to a given fraction of a cell burning. The banded nature of the plot in Figure ES-1b is due to the small averaging window size which is using only 25 pixels which leads to 25 discrete possibilities for the fraction of a cell that can be burning. As the grid cell size increases (Figures ES-1c and d), fewer instances of the entire cell burning are observed as the ignition patterns for the prescribed fires favored more backing and flanking fire behavior leading to the depth of the flaming front often being below the resolution of the computational grid. As the grid cell size increases, so does the likelihood that multiple processes are occurring below the model's ability to resolve them. One such process would be the drying of fuel prior to its ignition.

Currently in FIRETEC, subgrid processes such as combustion and fuel drying are tightly coupled through the PDF for fraction of a cell burning. This tight coupling limits the range of potential responses of the model to varying conditions. To relieve this limitation, the two processes are

coupled through a new set of equations describing the evolution of the variation of gas temperatures and both wet and dry solid temperatures. This new set of equations incorporates conservations of mass and energy for the dry and wet fuels, individually, to ensure the model can better represent sub-grid combustion and evaporation processes simultaneously.

The new equations are incorporated in a simulation and compared to observations (Figure ES-2), where the dashed lines are the mean temperatures of the various burning observations within the 1x1m cell, the red solid line with squares indicates modeled mean dry temperature, the blue solid line with circles is mean wet fuel temperature, the grey line is gas temperature and shading indicates one standard deviation above and below the mean based on the dry and wet modeled variances. While the observed fuel temperatures are significantly hotter than the modeled mean temperatures, if we truncate the simulation data (from the modeled mean temperature and variance) to values in the distribution greater than 773 K, we observe a significant improvement in the alignment between modeled and observed temperature, especially after the peak temperature as shown by the solid black line. Distinct differences include a more rapid modeled rise in temperature during the initial combustion phase with a slightly premature drop in temperature as fuel is being consumed and a slower reaction rate.

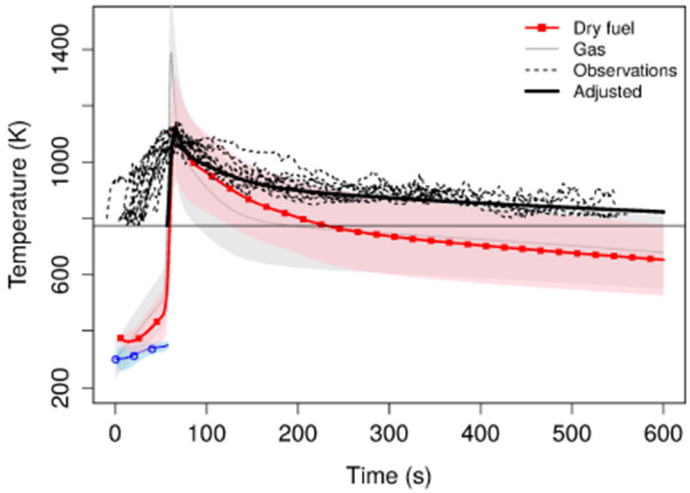

Figure ES-2: Simulation results for the mean wet solid fuel, dry fuel and gas temperatures (blue, red, grey solid lines) compared with observations (dashed lines) of mean solid temperature evolution in a 1 m x 1 m cell. The horizontal line is at 773 K (500 C) which is the minimum observed FLIR temperature. The adjusted dry fuel temperature (thick solid black line) is the recalculated mean temperature for temperatures above 773 K.

Implications for Future Research and Benefits

The focus of this project was improving the parameterization of the combustion process in coupled fire-atmosphere models by better describing the governing equations for wet and dry

fuels and their temperature evolution. Our future plan (currently ongoing) is to focus on the development of equations describing the evolution of the temperature variations for the gas phase based on a similar approach as described here. These new equations for the gas phase will then be coupled to the set of equations for the wet and dry fuels, which should improve the modeled energy exchange between wet and dry fuel and surrounding gas. This has a significant influence on fire behavior as we have previously shown. This energy exchange is one of the essential components contributing to the self-determining nature of FIRETEC.

The majority of fire model validation studies focus on comparing simulated fire perimeters to what was observed, most often for wildfires. While this may serve as a first cut at validation, it raises the question of whether the model is getting the right answer for the right reason. This study examined fuel moisture and temperature dynamics at the sub-meter scale to facilitate improved representations of combustion in fire spread models for lower-intensity fires where the heat transfer process is poorly resolved by the model grid. This focus on the lower end of the fire intensity scale will benefit Department of Defense land managers by improving model performance in conditions consistent with a wide range of prescribed fire applications.

Introduction

Wildfire behavior and spread are influenced by many complex processes involving the interactions between the fire and its surroundings. These interactions depend heavily on the dynamic and heterogeneous turbulent flow fields that connect fire to the fire environment, surrounding atmosphere, fuels (dead and live vegetation), and topography. Current physics-based fire behavior models leverage computational fluid dynamic (CFD) techniques to represent the coupled fire-atmosphere interaction using partial differential equations. These formulations describe the exchange of mass, momentum, and energy through non-linear processes such as convective and radiative heating and cooling, drag, turbulence, combustion, and evaporation (Linn 1997; Linn *et al.* 2002; Mell *et al.* 2007, 2009; Accary *et al.* 2014). Since wildland fires (wildfires and prescribed) occur at large spatial scales (hundreds of meters to hundreds of kilometers) and involve complex non-linear processes occurring at a wide variety of scales (e.g., atmospheric eddies hundreds of meters wide and reactions occurring in millimeter-diameter conifer needles), it is not currently feasible to resolve important phenomena over all relevant scales. Thus, to simulate wildland fires at landscape scales (100s of meters to kilometers or larger), compromises on the resolution of fine-scale processes and variations must be made and models or parameterizations must be developed to capture the net effects of sub-grid phenomena. This need is analogous to the development of turbulence closure models that capture the net effects of variations in a flow field that cannot be resolved.

Many recent CFD-based wildfire studies have focused on understanding the behavior of intense wildfire scenarios. These cases pose significant risks to people, communities, and infrastructure and are the most challenging to manage. The characteristic length scales of dominant fire phenomena (e.g. flame length) and fire geometry (e.g. fireline depth) typically increase with the intensity of the fire. Simultaneously, the sensitivity of fires to fine-scale variations in the ambient environment (e.g. turbulence or fuel heterogeneity) and the significance of fine-scale variations in fire conditions (e.g. temperature or moisture variations) decreases with the increase in the characteristic length scales. When conditions are extreme and fires are intense, existing physics-based wildfire behavior models typically perform well (e.g., Hoffman et al. 2016) since the dominating processes can generally be resolved and the impacts of sub-grid heterogeneities in temperature, wind, turbulence, fuel, and moisture are less significant. The conceptual diagram of fire and fuel within a single computational cell for high-intensity fire is shown in Figure 1a. However, the spatial scales of fire behavior are smaller and the importance of finer scale variations in fire activity and fire environment is greater during lower-intensity fires (Jonko et al. 2021; Linn et al. 2021; Parsons et al. 2011; Zhou et al. 2005). As the relevant length scales of the fire decrease relative to feasible model resolution, many physical wildfire behavior models struggle in this regime. For example, there can be significant heterogeneity in temperatures of both gases and solids within resolved volumes under these marginal conditions (hotter and cooler regions with respect to the mean resolved temperature) as is illustrated in Figure 1b. Capturing the influences of this heterogeneity is important as it directly relates to the drying and combustion processes and thus the spread of fires. The increasing desire to use prescribed fire

at the landscape scale will require tools capable of simulating all aspects of fire behavior, including flanking and backing fires, and their respective impacts on the ecological effects of fires.

(a) (b)

Figure 1: Conceptual images of a) length scales and cell level near homogeneity in high-intensity fire and b) length scales and cell level heterogeneity in low-intensity fire within a single computational grid cell. Figure a) photo credit: Rex Hsieh, FP Innovations (Pelican Mountain; Thompson et al. (2020)) and Figure b) photo credit: Ginny Marshall, Natural Resources Canada.

Physics-based coupled fire atmosphere models, such as FIRETEC (Linn 1997; Linn et al. 2002), use a series of coupled partial differential equations to track the evolution of mass, momentum, energy, turbulence, and species of the gases moving around a fire and the mass, moisture content, and temperature of the fuel (dead and live vegetation). In FIRETEC, as well as other similar models such as the Wildland Fire Dynamics Simulator (Mell et al. 2007, 2009), the solution of these coupled partial differential equations is done numerically on a three-dimensional grid. Typical grid sizes for simulations of kilometer-scale simulations are on the order of meters. The temperature and moisture variations that govern some ignition and drying processes can thus be explicitly resolved on meter scales, but even at the sub-meter scale, there can be distributions of temperatures and moisture contents. Currently, FIRETEC employs the notion of a probability distribution function (PDF) of temperatures within each grid cell to determine the moisture evaporation and combustion rates. Using this approach, FIRETEC avoids having a step function in the rate of evaporation or combustion associated with the mean temperatures reaching critical values such as evaporation and combustion temperatures. Instead, accounting for the existence of a distribution of temperatures allows for a crude representation of the fact that a small fraction of the fuel might be hot enough to evaporate water or begin to combust. This approach has

shown promise for some high-intensity fire scenarios based on model agreement with observations. However, the current formulation, which assumes a static subgrid temperature distribution shape, still presents challenges for low-intensity fire scenarios. In such cases, the scales for moisture and temperature heterogeneity are even more poorly resolved. As the importance of fine-scale variations increases with decreasing physical scales of the fires (lower intensity), the need for a more dynamic and scenario-dependent representation of sub-grid distributions becomes more apparent.

The current FIRETEC formulation explicitly tracks a mean solid fuel temperature and allows an assumed temperature variance. The combination is used to determine how much of the fuel is hot enough to evaporate water and to begin combusting as the temperature of the mean fuel increases. For example, by including the notion of the distribution of temperatures within a cell (some hot locations and some that might be still at ambient) water will start being evaporated while the mean temperature is well below 373 K. What is currently missing is a scenario-dependent methodology for determining the width of the distribution, which will be determined by environmental factors such as wind speed, gas temperature variation, and even initial moisture content levels. Simultaneous processes may be occurring within a single computational cell, in which water evaporates from wet fuel to produce dry fuels, while at the same time dry fuels may be subject to pyrolysis and combustion (Figure 2). In lower-intensity fire regimes, where the coincidence of drying and combustion occurring in the same cell increases, it is challenging to represent the influences of temperature distributions with a single energy equation for the solid fuel.

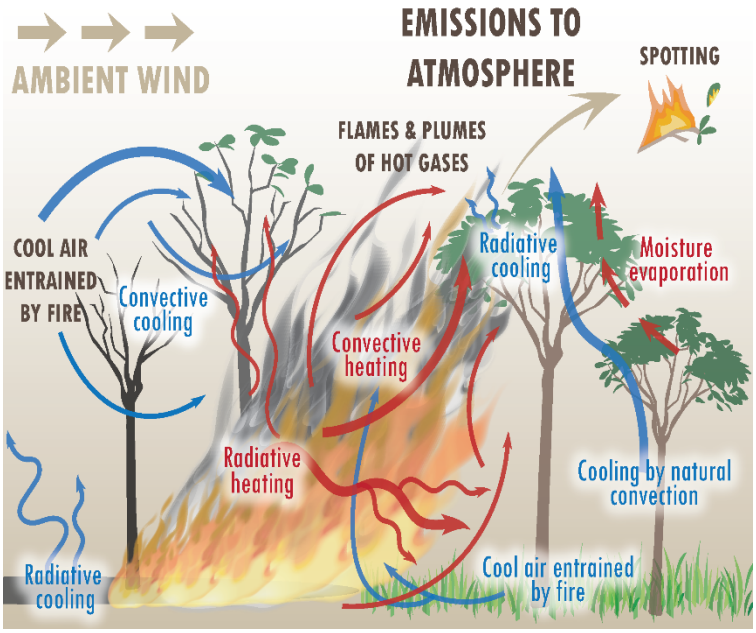

Figure 2: Illustration of physical processes governing the spread of wildland fires.

The overall goal of this project was to improve the representation of subgrid-scale processes in coupled fire-atmosphere models operating at the landscape level through the use of fine-scale infrared remote sensing at the plot level. As the governing equations for these models describe changes in model variables averaged over a grid volume, the measurements need to be amenable to similar averaging. Infrared remote sensing along with some additional measurements of the ambient environment allows us to track the temporal evolution of fuel temperature and fuel moisture flux in heterogeneous fuel beds at a sub-meter scale, ideal for evaluating subgrid scale combustion processes in the coupled model.

Methodology

The focus of this study is to improve our understanding of how subgrid processes influence the combustion process in FIRETEC. In each burning cell, the local reaction rate (average reaction rate within the cell) is described in terms of the change in bulk density of fine fuel particles, ρ_f, with time, t, and is captured by the following equation.

$$\frac{\partial \rho_f}{\partial t} = C_m \rho_f \rho_o \psi \sigma \lambda \qquad (1)$$

where C_m is a dimensionless reaction rate constant, ρ_f and ρ_o are the local bulk density [kg m^{-3}] of fine solid fuel (fine-scale biomass particles such as foliage or small twigs) and oxygen respectively. ψ is the fraction of the fuel in the computational cell that is actively burning, σ is the turbulent mixing coefficient, and λ is the dimensionless stoichiometry factor. Currently, in FIRETEC, ψ is defined as a probability distribution function (PDF) of temperatures within each grid cell to determine the fraction of a cell combusting for calculation of both moisture evaporation and combustion rates. Assessing how well this PDF performs requires fine-scale estimates of temperature to be able to estimate a measured analog to the model's PDF. Additionally, to guide any refinement of the parameterization, we also obtain additional fine-scale measurements to help us understand the system. These additional measurements include estimates of the reaction rate, fluxes of moisture, and flow field measurements to provide estimates of the turbulent mixing term in the reaction rate. Understanding these fine-scale processes will guide improvements to the parameterization of the reaction rate.

Thermal Imagery

We used an S60 longwave infrared (LWIR) thermal imaging system from FLIR Inc. (Wilsonville, OR) for the thermal data. The S60 uses a focal-plane array uncooled microbolometer with a resolution of 320x240, a spectral range of 7.5–13 μm, a sensitivity of 0.068C, a spatial resolution of 1.3 mRad, and a thermal accuracy of ±2%. The measurements were captured from an 8.2-m tall tripod designed to provide a nadir perspective. The tripods were positioned over pre-surveyed 4x4 m plots as described in O'Brien et al (2016). The height of the nadir-view tripod system provided a 4.8x6.4m field of view for the S60 camera.

The FLIR systems gave radiometric temperatures in °C as raw output. For all LWIR imagery, the native file format was converted to an ASCII array of temperatures in °K with rows and columns representing pixel positions. Temperatures were then converted into W m^{-2} (fire radiated flux density; FRFD) using the Stefan–Boltzmann equation for a grey body emitter assuming an emissivity of 0.98. Residence times were also calculated as the amount of time a pixel was measured to be above the Draper point (525°C) among all pixels in the burn block for the duration of the event and maximum residence time was the maximum number of times a single pixel was measured to be above the Draper point. Our technique likely underestimates the contribution of flames to power and energy release because of low flame emissivity (Johnston et al. 2014) and flames having their peak emissions in the midwave portion of the infrared spectrum; however, our methodology does accurately capture temperatures of the burning fuel and heated soil which is a better match for comparisons with fuel temperatures from the model. For estimating the fractional area burning, the fraction of pixels above the Draper point within an analysis block was used. The size of analysis blocks was varied from 2 cm^2 up to 4 m^2 to assess possible model resolution influences on the ψ function.

Mass Loss Rate

Thermal remote sensing of active biomass fires provides a pathway for providing spatially and temporally explicit estimates of fuel consumption by building a relationship between fire radiative energy and fuel mass loss (Wooster et al 2004). It has been demonstrated that fire radiative energy is linearly related to the total amount of fuel consumed, and that fire radiative power is linearly related to the rate of fuel consumption in a statistically significant manner (Wooster, 2002; Wooster et al., 2005). Freeborn et al (2008) utilized infrared remote sensing in a laboratory setting to evaluate relationships between energy release, fuel mass loss, and emissions with good success. Loudermilk et al (2012) employed infrared thermography to explore links between fuel structure and fire behavior at fine scales in natural fuel beds.

We have adapted the methodology of Freeborn et al. (2008) to the field measurements of Loudermilk et al. (2012) to provide a detailed view of fuel consumption. As expected, a linear relationship was found between energy release and fuel consumption (Figure 3). The relationship was developed in the lab by direct measurement of mass loss rate by burning on a digital scale

and tracking both the change in mass with the scale and changes in fuel temperature using the FLIR (Figure 4). The relationship proved to be sufficiently robust when the experimental setup was moved from lab conditions to the outdoor environment.

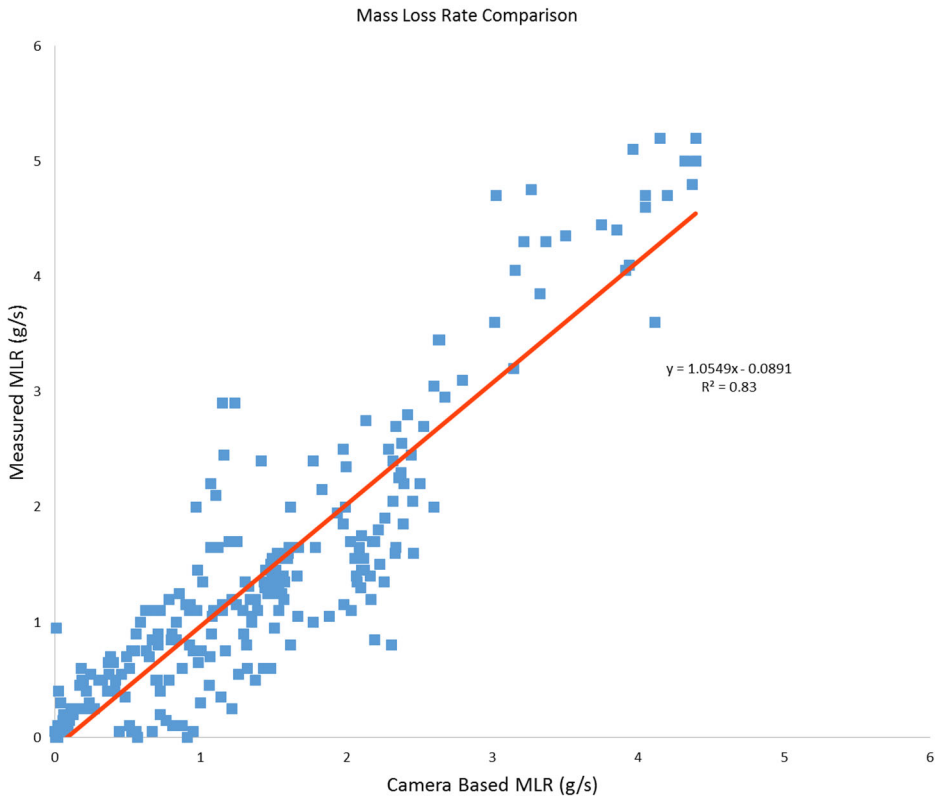

Figure 3 Scatter plot comparing observed and predicted mass loss rates.

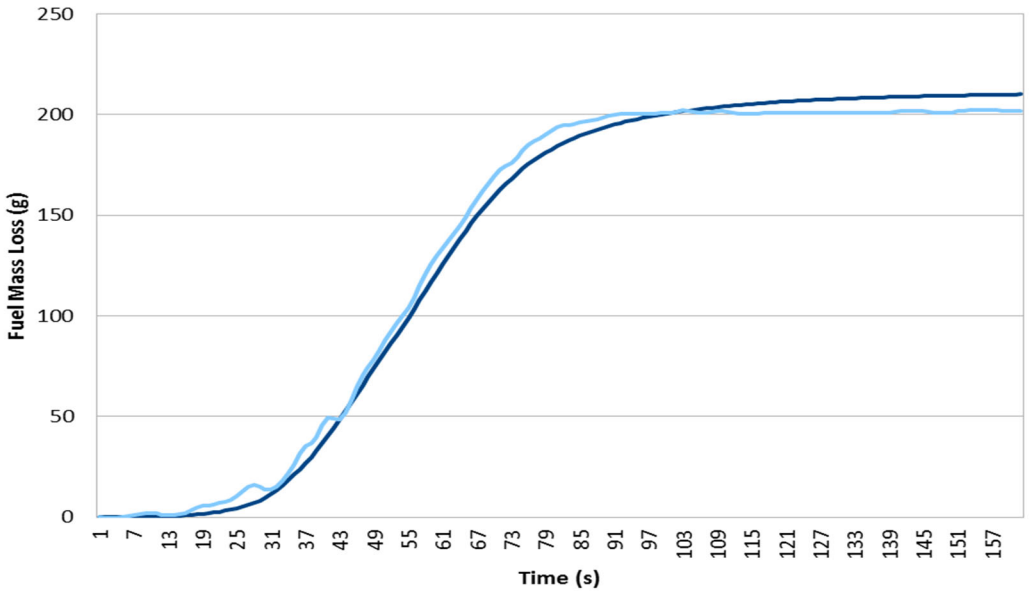

Figure 4 Cumulative mass loss curve for laboratory experiment (light blue line is estimated mass loss from imagery and dark blue is mass loss measured with the scale).

Fuel Moisture Dynamics

For years the numerical weather prediction community has been using satellite-derived surface temperature tendencies to estimate surface moisture content and constrain the surface energy budget within mesoscale weather models (McNider et al 1994). There have been numerous studies linking fuel moisture to various satellite-based vegetation indices such as the normalized difference vegetation index (NDVI) (e.g., Caccamo et al 2012). A key component of these vegetation indices is the use of a measurement band in the infrared part of the spectrum.

Our project sought to adapt the methodologies of McNider et al (1994) to the problem of estimating fuel moisture. Surface temperature trends along with other meteorological measurements would be used with the surface energy balance to estimate the magnitude of the moisture flux from the vegetation (Figure 5). The complexity of additional measurements along with the additional measurement uncertainty resulted in less-than-desirable results. As an alternative, a new method was developed that involved the introduction of several targets of known radiative properties (Figure 6). Fuel temperatures exhibit a response similar to the white targets when moisture is present and as the fuels dry the fuel temperatures track closer to the black targets (Figure 7).

The targets streamline the calculation process. Rather than requiring a pyranometer for estimating solar radiation and using optical flow techniques to estimate the flow field to aid in estimating the sensible heat term of the energy budget, we now use a system of three energy budget equations: one for the fuels and one for each of two targets. The targets are designed to have similar aerodynamic properties as the vegetation but each target has a different known

albedo. Since the targets lack moisture, their energy budgets lack the latent heat flux term, and the aerodynamic similarity results in a system of three equations with three unknowns: incoming solar radiation, sensible heat flux, and latent heat flux for the fuels. Figure 7 shows the targets, made from aluminum ovals (1x2 cm) and painted with high-temperature paint (either black or white). Pixels for targets are identified by matching locations in visual images with pixel locations in the IR images.

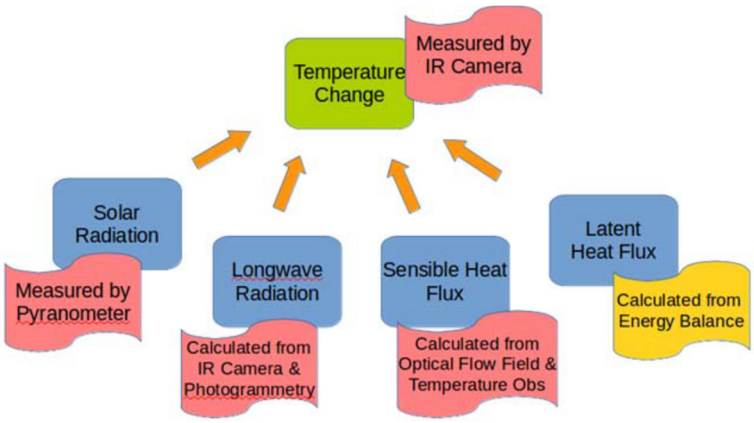

Figure 5 Original conceptual model for determining fuel moisture content from remotely sensed IR data combined with other environmental measurements

Figure 6. Targets used for moisture flux estimation.

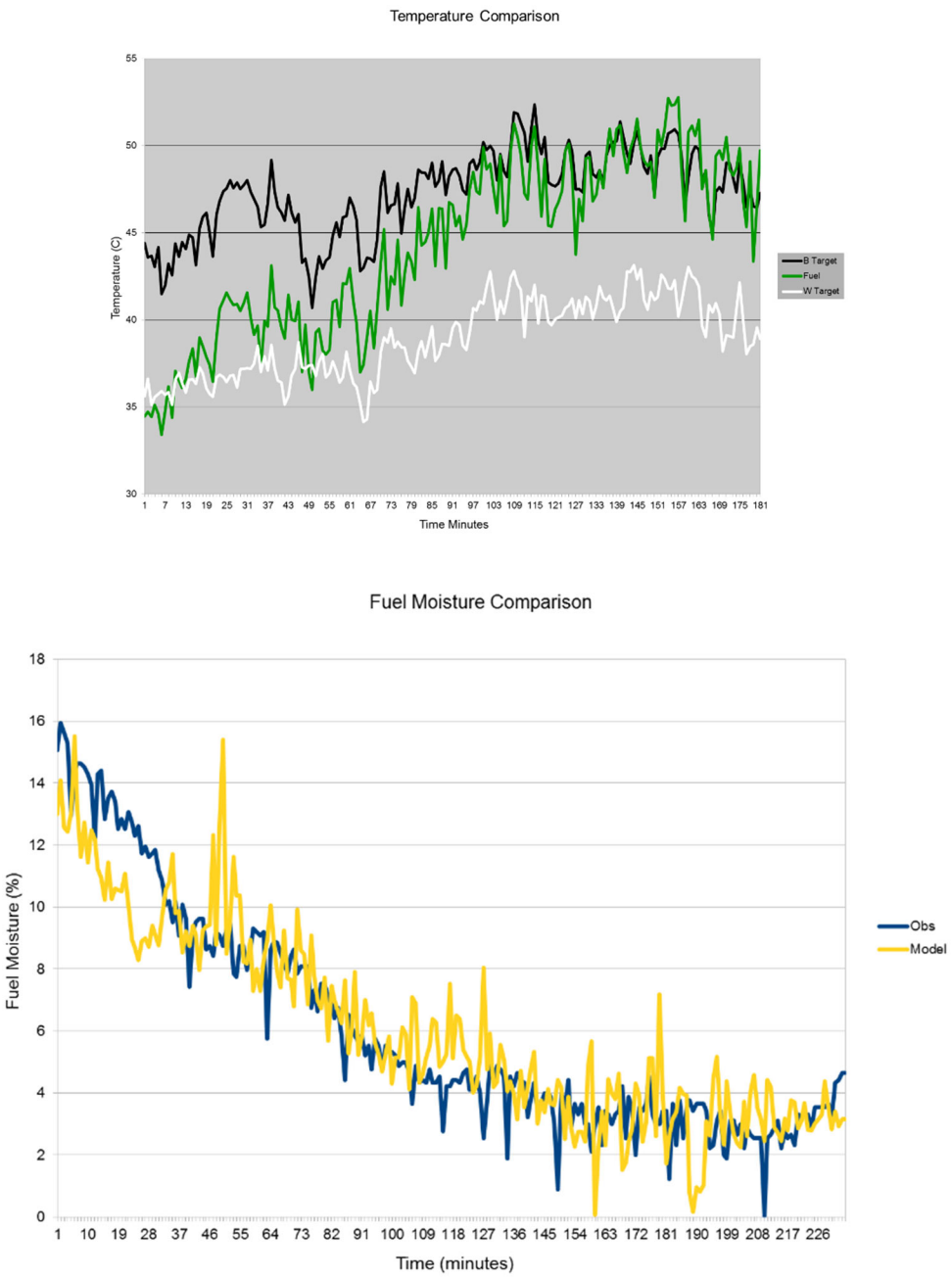

Figure 7 Comparison of fuel and target temperatures (top) and model versus observed moisture content

Optical Flow

To obtain information on fire-induced flow, additional visual imagery was captured by a GoPRO HERO3 camera collocated with the FLIR system on the tripod. Resolution of the video imagery is 1920 × 1080 pixels and was captured at a frame rate of 30 fps. The flow field in the vicinity of the fire was estimated by applying cross-correlation particle image velocimetry (PIV). Our PIV

implementation was inspired by the work of Fujita and Hino (2003), who used an unseeded PIV method to estimate river flows. In their work, Fujita and Hino had intended to use the unseeded PIV measurement technique for small ripples, resulting from wall-bounded turbulence, on the water surface. Instead, they used the method for large-scale patterns, caused by the interaction of boil vortices generated near the river bed with the water surface, which typically occurs in high river-flow conditions. This choice was a consequence of video images being taken from a helicopter, which made it difficult to capture small ripples on the water surface. In the current study, the unseeded PIV measurement technique could be applied in slow-flow conditions since the camera was located relatively close to the fuel bed, i.e. at a height of 8.2 m. While the methodology of Fujita and Hino relied on patterns generated by the interaction of boil vortices with the water surface as natural unseeded tracers, we have relied on patterns generated by the fire-flames, smoke, and ash particles as our unseeded tracers. Next, the cross-correlation PIV was implemented in Python using the openpiv module (Python version 3.8.5 and Anaconda environment version 4.9.2). The interrogation window was set at 24 pixels with a window overlap of 12 pixels and a search-area size set as 2.5 times the interrogation window size. The video from the GoPRO camera was trimmed to a 2.34 m × 2.34 m area in the center of the burn area for an image size of 888 × 888 pixels, and split into sequential images with a time step of 1/30 of a second. A sample of the PIV output is shown in Figure 8 for a simple point ignition in calm conditions.

Our goal with these measurements was to develop and demonstrate techniques for collecting sub-meter scale measurements suitable for investigating the subgrid parameterization of a range of physical processes within a coupled fire-atmosphere model such as FIRETEC. While our focus in this study is the parameterization of the combustion process and specifically the form of a PDF used in that parameterization, our measurements extended beyond what was needed to investigate that specific parameterization by including estimates of moisture fluxes and turbulent flow dynamics to foster a more holistic understanding of subgrid processes that will lead to further investigations.

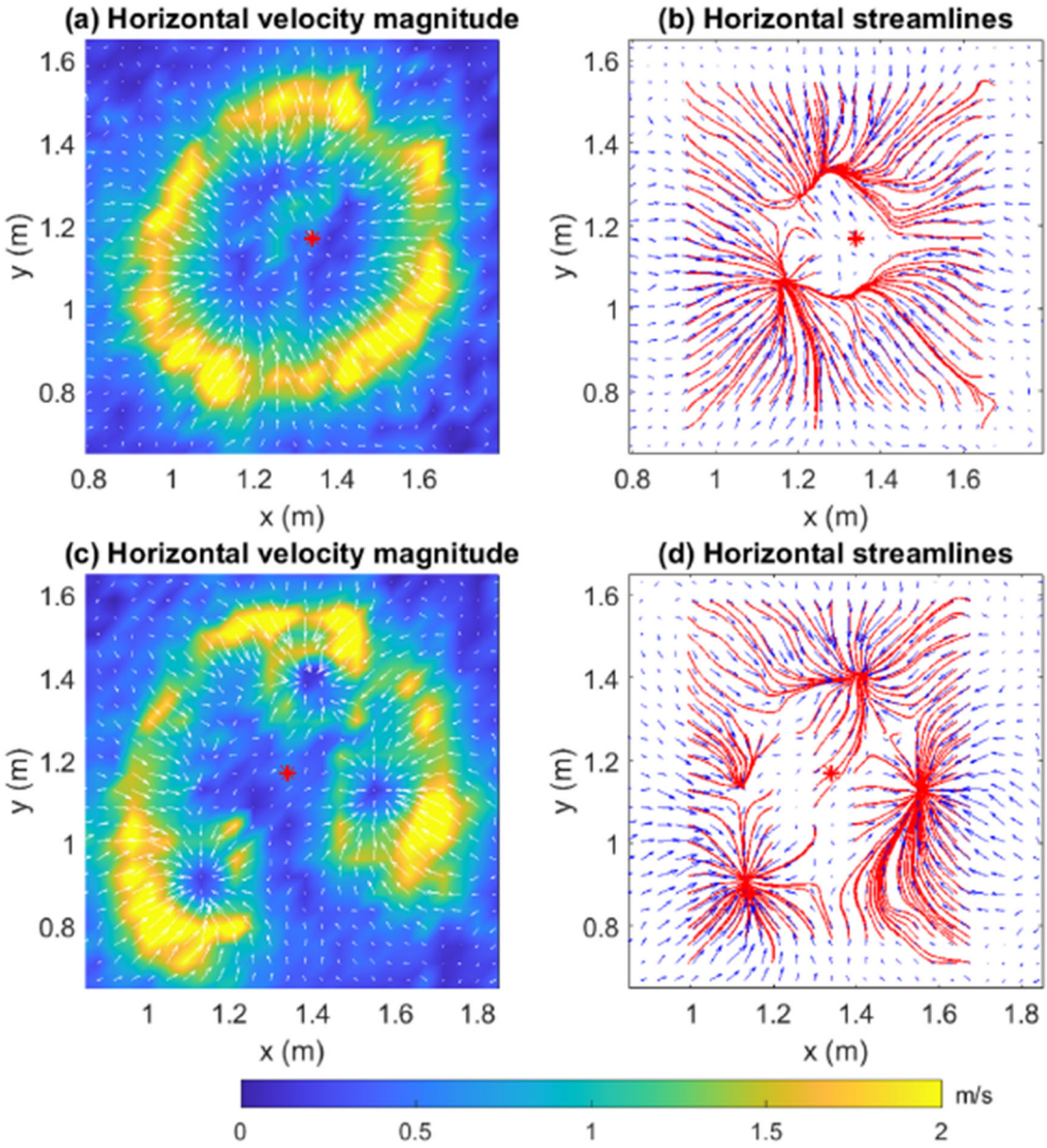

Figure 8. Example horizontal velocity vectors overlaid on color contours of the velocity magnitude with streamlines overlaid on horizontal velocity for a point ignition after 100 seconds (a,b) and 110 seconds (c,d).

Formulation of revised PDF

The intent of the ψ function in equation 1 is to provide an estimate of the fraction of a computational cell burning as a function of the cell's mean temperature. Using the Draper point as the transition point between burning and not burning, the pixels of each image from the FLIR system can be transformed into a binary image of pixels burning and not burning. Various size

averaging windows can then be applied to both images to determine the mean temperature within the averaging window and the fraction of pixels within the window that are burning, thus providing an estimate of ψ (Figure 9).

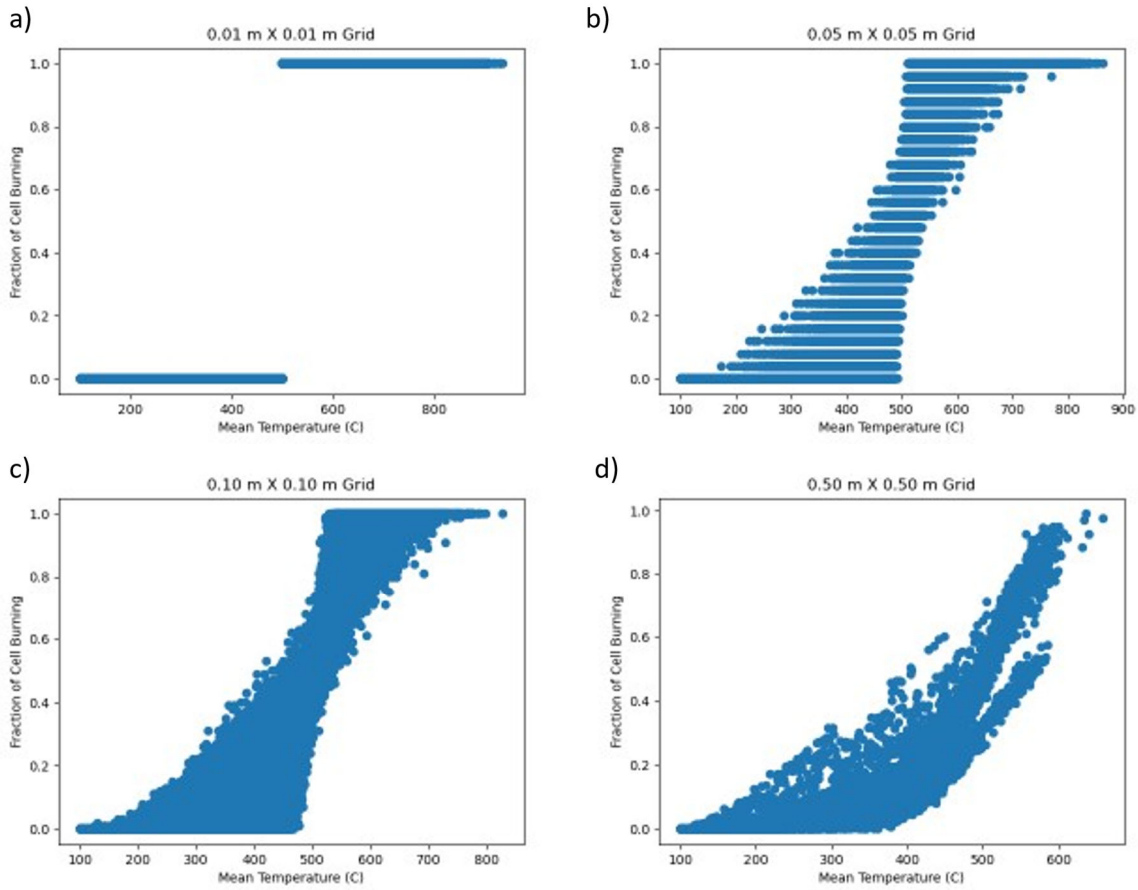

Figure 9. Fraction of computational cell burning as a function of mean temperature derived from FLIR imagery for grid sizes of a) 0.01m, b) 0.05m, c) 0.10m, and d) 0.50m.

The finest scale used in Figure 9a is at the pixel resolution of the camera which yields a step function as cells are either burning or not, but increasing the resolution by a factor of 5 (Figure 9b) yields a broad range of mean temperatures that can correspond to a given fraction of a cell burning. The banded nature of the plot in Figure 9b is due to the small averaging window size which is using only 25 pixels which leads to 25 discrete possibilities for the fraction of a cell that can be burning. As the grid cell size increases (Figures 9c and 9d), fewer instances of the entire cell burning are observed as the ignition patterns for the prescribed fires favored more backing and flanking fire behavior leading to the depth of the flaming front often being below the resolution of the computational grid. As the grid cell size increases, so does the likelihood that

multiple processes are occurring below the model's ability to resolve them. One such process would be the drying of fuel prior to its ignition.

Currently in FIRETEC, subgrid processes such as combustion and fuel drying are tightly coupled through the PDF for fraction of a cell burning. This tight coupling limits the range of potential responses of the model to varying conditions. To relieve this limitation, the two processes are coupled through a new set of equations describing the evolution of the variation of gas temperatures and both wet and dry solid temperatures. This new set of equations incorporates conservations of mass and energy for the dry and wet fuels, individually, to ensure the model can better represent sub-grid combustion and evaporation processes simultaneously.

Equations for Temperature of Wet and Dry Fuel

Critical processes governing the spread of wildland fire depend on the temperature of the combustible material. In most natural scenarios the fuel is initially a combination of combustible biomass and water. Fuel moisture fraction, defined as the mass of water divided by the mass of the oven-dried combustible biomass (or moisture content which is the moisture fraction written as a percent) influences the temperature dynamics of combustible material because it adds significant thermal mass to the fuel and becomes an energy sink associate with the evaporation of water. The initial water content of live fuels depends largely on the plant's physiological processes, which respond to a variety of environmental factors, and available water in the ground (Jolly et al. 2014). The ambient water content of the dead fuel is a dynamic quantity that depends on the history of the local humidity and the size and shape of the biomass. Fine fuels equilibrate with the atmospheric moisture levels rapidly (< 1 hour), whereas thicker fuels take 10s, 100s, or even thousands of hours to equilibrate (van der Kamp et al. 2017). Since wildland fire spread is heavily dependent on fine fuels such as foliage, grasses, or twigs our attention is currently focused on the dynamic conditions of this subset of the biomass, but future work will be needed to include larger fuels in this formulation as they are important for determining fire emissions, fire effects, and the sustaining of ignitions.

An equation for the evolution of the temperature of the solid (combustible fuel and associated water content) at a single point can be achieved by beginning with the equation for the conservation of the internal energy of the solid. Then we subtract the conservation of mass equation multiplied by the temperature of the solid, T_s, and specific heat, c_{ps}. For this purpose, the biomass and water content temperatures are assumed to be the same and the specific heat of the solid is a mass-weighted average of the combustible fuel and water. Equations of this sort are currently used in physics-based wildland fire models such as FIRETEC, as is shown in equation 2 (Linn et al. 2002; Linn & Cunningham 2005). In this equation, the bulk density of the solid, ρ_s, is treated as the sum of the bulk density of water, ρ_{H2O}, and fuel, ρ_f . The combined internal energy of the fuel and water is the product of ρ_s, T_s, and a mass-weighted specific heat, c_{ps} which combines the specific heat of water, c_{pH2O} , and the specific heat of the combustible fuel, c_{pf} .

$$c_{p_s}\rho_s\frac{\partial T_s}{\partial t} = q + ha_v(T_g - T_s) + F_f(H_f\Theta - c_{p_f}T_{crit}N_f) - F_{H_2O}(H_{H_2O} + c_{p_{H_2O}}T_{vap}) \quad (2)$$

In the above formulation, q is the net radiation heat transfer rate per unit volume, h is the convective heat transfer coefficient, a_v is the area per unit volume of the fuel in a cell, T_g is the local temperature of the gas, F_f is the mixing-limited reaction rate as described by Linn (1997), H_f is the heat of combustion of the fuel, Θ is the fraction of the reaction energy that is deposited directly back to the fuel, T_{crit} is a critical local temperature for pyrolysis (taken to be 600K in this manuscript), N_f is a stoichiometric coefficient for the net burning reaction as described by Drysdale (1985), F_{H2O}, is the rate of water evaporation, H_{H2O} is the heat of vaporization of liquid water, and T_{vap} is the temperature of water vaporization at standard pressure. For a single location, F_{H2O} only has a non-zero value when the temperature of that location is T_{vap} and above this temperature, the moisture content is zero. F_f is assumed to begin at the critical temperature, but it can persist at higher temperatures since combustion depends on other factors, such as oxygen concentration and mixing.

There are challenges associated with applying this equation in numerical simulations, where computations are not performed at every single point but are instead used to describe the mean temperature in a control volume or computational cell. In the case of models designed for landscape-scale fires, length scales in these control volumes can be on the order of meters. In such volume sizes, there can be a mixture of states that are not explicitly resolved (Linn 1997). For example, it is possible to have fuel that is wet, drying, dried and heating up, and combusting all in the same computational cell, especially in the context of low-intensity fires. In an attempt to account for the fact that there was likely a range of temperatures within the control volume, the concept of temperature distribution or probability distribution function (PDF) was introduced (Linn 1997) in the reaction rate and later to the moisture evaporation. This concept, which captures the presence of both warm and cold regions within a volume, allowed moisture to begin to evaporate before the mean temperature reached vaporization temperature and for combustion to start even before all of the moisture was evaporated. This approach has shown many benefits. In the original formulations, however, there was no mechanism that allow for the PDF width or shape to dynamically evolve based on the fire environment. This presents challenges to the generality of the model and its applicability to portions of low-intensity fires.

In order to increase the generality of this approach, it is necessary to incorporate a dynamic PDF that adapts to the fire environment. However, initial attempts to derive the governing equations for the dynamic width, or standard deviation, of the probability density function for the solid temperature distribution ran into challenges related to the phase change threshold associated with moisture evaporation. The equations for a variance of the temperature distribution were tractable for temperatures above and below the temperature of evaporation. In this original formulation, the amount of moisture associated with the fuel was tracked, but the amount of fuel that was still wet (below evaporation temperature) and the amount of fuel that was dry (at

least momentarily above the evaporation temperature could potentially rise to combustion temperatures) were not explicitly and separately tracked. In order to better track the distribution of temperatures, evaporation of water, and the potentially simultaneous combustion processes that occur within a control volume, we develop a new approach for the individual evolution of wet and dry solids.

For this new approach, we partition the solid fuel into two categories or states; wet and dry. Wet fuel is the fuel that has the initial moisture content (determined by the ambient conditions before a fire arrives at the location) and dry fuel is the biomass that has had the moisture driven off as a result of heating by the fire. Using this construct, the bulk density of the fuel-moisture mixture, ρ_s, is the sum of dry fuel, ρ_d, and wet fuel, ρ_w, and water, ρ_{H2O}. This is illustrated in equation 3, where wet fuel and water can be combined to obtain the bulk density of the wet solid, that is $\rho_{sw} = \rho_w + \rho_{H2O}$,

$$\rho_s = \rho_d + \rho_w + \rho_{H_2O} = \rho_d + \rho_{sw}. \tag{3}$$

The conceptual division between wet and dry fuel is based on the notion that fuel is initially wet and then it is dried to generate dry fuel. We assume that all fuel within a control volume has the same initial moisture fraction, or ratio, r_{moist} ($r_{moist} > 0$), which remains constant for the wet fuel. Furthermore, there is initially no dry fuel since even dead fuels have a non-zero equilibrium moisture content with the atmospheric humidity. Thus, the bulk density of the wet solid is the same as the bulk density of the solid, $\rho_{sw} = \rho_s$, at the initialization.

With this in mind, the conservation of mass equations for the water and the wet fuel based on the rate of evaporation of water per unit volume, F_{H2O}, are:

$$\frac{\partial \rho_{H_2O}}{\partial t} = -F_{H_2O} \tag{4}$$

$$\frac{\partial \rho_w}{\partial t} = -\frac{F_{H_2O}}{r_{moist,w}} \tag{5}$$

where the moisture fraction of the wet solid is given by:

$$r_{moist,w} = \frac{\rho_{H_2O}}{\rho_w}. \tag{6}$$

The term $r_{moist;w}$ must be greater than zero since the wet solid fuel will never be completely dry, but $r_{moist;w}$ can be larger than one which simply indicates that the mass of the water is larger than the mass of the biomass. For example, a live deciduous leaf could have a moisture fraction of 2, meaning the mass of water contained in the leaf is twice that of the dry mass.

We assume that ρ_{H2O} approaches zero at a rate proportional to the rate at which wet mass becomes dry. Thus, $r_{moist;w}$ remains a constant even when water is completely evaporated. We can then form the conservation of mass of the wet solid and its moisture, ρ_{sw}:

$$\frac{\partial \rho_{sw}}{\partial t} = -F_{H_2O}\left(1 + \frac{1}{r_{moist,w}}\right), \tag{7}$$

where mass loss from the wet fuel conservation equation corresponds to a mass source in the conservation of dry fuel equation:

$$\frac{\partial \rho_d}{\partial t} = -F_f N_f + \frac{F_{H_2O}}{r_{moist,w}}. \tag{8}$$

The additional sink term in equation 8, that is $-F_f N_f$, corresponds to the mass loss rate due to the burning of dry fuel. Using the definition of the two different categories of solids, we can then write conservation equations for the internal energy of both wet and dry solids respectively,

$$\frac{\partial c_{p_{sw}} \rho_{sw} T_w}{\partial t} = q_w + h a_{v,sw}\left(T_g - T_w\right) + F_f H_f \Theta_w - F_{H_2O}\left(c_{p_{H_2O}} + \frac{c_{p_f}}{r_{moist,w}}\right) T_{vap} - F_{H_2O} H_{H_2O} \tag{9}$$

and

$$\frac{\partial c_{p_f} \rho_d T_d}{\partial t} = q_d + h a_{v,d}(T_g - T_d) + F_f H_f \Theta_d + F_{H_2O}\frac{c_{p_f}}{r_{moist,w}} T_{vap} - F_f N_f c_{p_f} T_{combust} \tag{10}$$

where $c_{psw}\ \rho_{sw} = \rho_{H2O}\ c_{pH2O} + c_{pf}\ \rho_w$, Θ_w and Θ_d are the fractions of combustion energy that is directly deposited on the wet and dry solid respectively, $T_{combust}$ is the temperature at which combustion occurs and solid fuel mass is converted to gaseous products, and h is the convective heat transfer coefficient, which is assumed to be the same for wet and dry materials given they are the same shape and size. $A_{v;sw}$ and $a_{v;d}$ are the area per unit volume of the wet and dry fuel, which are calculated based on their respective bulk density, ρ_x, the material density, ρ_{micro}, and size scale (radius of cylindrical fuel particles), s_s; of the fuel particles:

$$a_{v,x} = \frac{2\rho_x}{s_s \rho_{micro}} \tag{11}$$

where the subscript *x* indicates either wet fuel (abbreviated *sw*) or dry fuel (abbreviated *d*) bulk density.

In both equations 9 and 10, the first terms on the right side of the equation are net radiation, the second terms are convective heat transfer, and the third terms are deposition of energy deposited via the combustion processes. The fourth terms on the right side of these equations

represent the transfer of energy associated with the movement of mass from the wet state to the dry state and the loss of the mass of the water from the wet state. The final terms in wet internal energy equation (Eq. 9) represent the endothermic evaporation process. It is important to note that the evaporation rate goes to zero as the density of wet fuel goes to zero. The final term in the dry internal energy equation (Eq. 10) accounts for energy loss from the dry state due to the mass losses associated with gaseous products in the combustion process.

We can now assume that the specific heat of the wet fuel does not change significantly with temperature since the moisture fraction remains the same until wet mass is transferred to dry state. Based on this assumption, if we subtract the product of specific heat, temperature of wet fuel, and the conservation of wet mass equation, that is

$$c_{p_{sw}} T_w \frac{\partial \rho_{sw}}{\partial t} = -F_{H_2O} \left(c_{pH_2O} + \frac{c_{p_f}}{r_{moist,w}} \right) T_w, \tag{12}$$

From equation 9, we arrive at:

$$\begin{aligned} c_{p_{sw}} \rho_{sw} \frac{\partial T_w}{\partial t} = {} & q_w + h a_{v,sw} (T_g - T_w) + F_f H_f \Theta_w - F_{H_2O} H_{H_2O} \\ & + F_{H_2O} \left(c_{pH_2O} + \frac{c_{p_f}}{r_{moist,w}} \right) (T_w \delta_w - T_{vap}) . \end{aligned} \tag{13}$$

In equation 13, δ_w (defined in Eq. 13) has been added to account for the fact that water evaporation only occurs when $T_w = T_{vap}$, which means that $F_{H2O} \neq 0$ when the wet solid temperature is T_{vap}. Thus, the final F_{H2O} term will cancel since we assume there is no evaporation when the temperature is below T_{vap}, and when any portion of the wet fuel reaches T_{vap}, the water is immediately evaporated. The newly dried fuel is now tracked in the dry fuel equation.

$$\delta_w = \begin{cases} 0, & T_w < T_{vap} \\ 1, & T_w = T_{vap}, \end{cases} \tag{14}$$

For the dry fuels, we similarly subtract the term $c_{p_f} T_d \frac{\partial \rho_d}{\partial t}$ defined as

$$c_{p_f} T_d \frac{\partial \rho_d}{\partial t} = -c_{p_f} T_d F_f N_f + c_{p_f} T_d \frac{F_{H_2O}}{r_{moist,w}} \tag{15}$$

From equation 10. Thus, we arrive at:

$$\begin{aligned} c_{p_f} \rho_d \frac{\partial T_d}{\partial t} = {} & q_d + h a_{v,d} (T_g - T_d) + F_f H_f \Theta_d + \frac{F_{H_2O}}{r_{moist,w}} c_{p_f} (T_{vap} - T_d) \\ & + F_f N_f c_{p_f} (T_d \delta_d - T_{combust}) . \end{aligned} \tag{16}$$

Analogous to δ_w in the wet temperature equation, δ_d is added, that is

$$\delta_d = \begin{cases} 0, & T_d \neq T_{combust} \\ 1, & T_d = T_{combust}. \end{cases} \tag{17}$$

Thus, the last two terms in equation 15 now cancel each other. It is worth noting that $T_{combust}$ is not a fixed value, but it is the temperature at which combustion is taking place at any given location or instant.

The concept of wet and dry fuel for this formulation is associated with wet and dry fuel particles or even wet and dry sections of the length of fuel particles in the case of thin fuels, which is our focus here. In future formulations, this can be expanded to handle gradients of moisture within thicker fuels as the outer shell can be dried while the inner core might still be wet. For the current case, however, we assume homogeneous temperatures and moisture fraction throughout the fuel particle thickness (thermally thin and moisture thin). The areas per volume of the wet and dry mass, $a_{v;sw}$ and $a_{v;d}$, can be related to an aggregate area per volume. That is if we assume that the difference in wet versus dry fuel is predominantly due to position in the cell (i.e., one spot has been dried out, while another spot is still wet),

$$a_{v,sw} = a_v \frac{\rho_{sw}}{\rho_d + \rho_{sw}} \tag{18}$$

and

$$a_{v,d} = a_v \frac{\rho_d}{\rho_d + \rho_{sw}}. \tag{19}$$

The fraction of combustion energy returning directly to the solid, Θ_s, can be split into a fraction that is deposited directly on the dry and wet fuels. In such a spatially segregated paradigm, however, we are in principle assuming that the energy returning to the solid is predominantly to the dry solid, where combustion is occurring. Thus, we approximate these terms as $\Theta_d = \Theta_s$ and $\Theta_w = 0$.

Mean Temperature Equations

To derive the equation for the mean temperatures of the wet and dry solids, we decompose the quantities of equations 13 and 16 into mean and fluctuating parts. Then, we take the ensemble average of these equations similar to the development of mean velocity equations in turbulence modeling (Daly & Harlow 1970). Thus, we get the following two expressions:

$$c_{p_f}\left(\overline{\rho_d}\frac{\partial\overline{T_d}}{\partial t}+\overline{\rho'_d\frac{\partial T'_d}{\partial t}}\right)=\overline{q_d}+\overline{h}\overline{a_{v,d}}\left(\overline{T_g}-\overline{T_d}\right)+\overline{h}\left(\overline{a'_{v,d}T'_g}-\overline{a'_{v,d}T'_d}\right)+\overline{a_{v,d}}\left(\overline{h'T'_g}-\overline{h'T'_d}\right)$$
$$+\overline{h'a'_{v,d}}\left(\overline{T_g}-\overline{T_d}\right)+\overline{h'a'_{v,d}T'_g}-\overline{h'a'_{v,d}T'_d}+\overline{F_f}(H_f\Theta_d)$$
$$+\overline{F_{H_2O}}\frac{c_{p_f}}{r_{moist,w}}[T_{vap}-\overline{T_d}]-\frac{c_{p_f}}{r_{moist,w}}\overline{F'_{H_2O}T'_d} \quad (20)$$

$$c_{p_{sw}}\left(\overline{\rho_{sw}}\frac{\partial\overline{T_w}}{\partial t}+\overline{\rho'_{sw}\frac{\partial T'_w}{\partial t}}\right)=\overline{q_w}+\overline{h}\overline{a_{v,sw}}\left(\overline{T_g}-\overline{T_w}\right)+\overline{h}\left(\overline{a'_{v,sw}T'_g}-\overline{a'_{v,sw}T'_w}\right)$$
$$+\overline{a_{v,sw}}\left(\overline{h'T'_g}-\overline{h'T'_w}\right)$$
$$+\overline{h'a'_{v,sw}}\left(\overline{T_g}-\overline{T_w}\right)+\overline{h'a'_{v,sw}T'_g}-\overline{h'a'_{v,sw}T'_d}$$
$$+\overline{F_f}H_f\Theta_w-\overline{F_{H_2O}}H_{H_2O}. \quad (21)$$

If we consider the solid density distribution or density variation to be somewhat dominated by the presence of, or their lack of, a fuel particle at a specific location and thus bimodal, then we can neglect $\overline{T'_d\rho'_d}$ terms. This implies that both positive and negative dry fuel temperature fluctuations exist, where there is fuel (positive density fluctuation), and neither are relevant in locations where there is no dry fuel. Additionally, if we assume that fuel particles do not change their radius while they burn, but rather shrink in their length (and local density) until they disappear, then the correlations between $a'_{v;d}$ and $a'_{v;sw}$ can be neglected. This approximation is consistent with previous work, in which the size scale of particles does not change with combustion, for example, Linn (1997) and Linn et al. (2002). Thus, the correlations between $a'_{v;d}$ and temperature are minimal even if the radius was changing. It is also reasonable to assume changes in the heat transfer coefficient are not due to changing solid temperature, but rather due to properties of the air, i.e., temperature or velocity. As a first approximation, therefore, we assign $\overline{h'T'_d}$ = 0 and $\overline{h'T'_w}$ = 0. Finally, we neglect third and higher-order correlation terms for this initial approach at the dynamic PDF for simplicity.

$$c_{p_f}\overline{\rho_d}\frac{\partial\overline{T_d}}{\partial t}=\overline{q_d}+\overline{h}\overline{a_{v,d}}\left(\overline{T_g}-\overline{T_d}\right)+\overline{a_{v,d}}\overline{h'T'_g}+\overline{F_f}(H_f\Theta_d)$$
$$+\overline{F_{H_2O}}\frac{c_{p_f}}{r_{moist,w}}[T_{vap}-\overline{T_d}]-\frac{c_{p_f}}{r_{moist,w}}\overline{F'_{H_2O}T'_d} \quad (22)$$

$$c_{p_{sw}}\overline{\rho_{sw}}\frac{\partial\overline{T_w}}{\partial t}=\overline{q_w}+\overline{h}\overline{a_{v,sw}}\left(\overline{T_g}-\overline{T_w}\right)+\overline{a_{v,sw}}\overline{h'T'_g}$$
$$+\overline{F_f}H_f\Theta_w-\overline{F_{H_2O}}H_{H_2O}. \quad (23)$$

These expressions are not in a closed form due to two terms: $\overline{h'T'_g}$ and $\overline{F'_{H_2O}T'_d}$. We now try to address this closure problem. Beginning with the covariance between the heat transfer coefficient and the gas temperature, we first consider the equation for the heat transfer coefficient used in FIRETEC, that is

$$h = (0.25)(0.683)Re^{0.466}\frac{\lambda_{air}}{s_s}, \tag{24}$$

as was described by Incropera and DeWitt (1996) for forced convection over tubes with the local Reynolds number defined as:

$$Re = \frac{Us_s}{\nu}. \tag{25}$$

In these equations, λ_{air} is the thermal conductivity of air, U is the local velocity (including contributions from mean and fluctuating components), s_s is the size scale associated with fuel particles, and υ is kinematic viscosity.

We utilize a simple linear relationship with gas temperature for both viscosity and conductivity, such that $\nu = C_1\bar{T}_g - C_2$ and $\lambda_{air} = C_3\bar{T}_g + C_4$., where $C_1 = 1.66\text{x}10^{-7}$, $C_2 = 3.37\text{x}10^{-5}$, $C_3 = 5.55\text{x}10^{-5}$, and $C_4 = 9.59\text{x}10^{-3}$. Incorporating these new equations into equation 23 we arrive at

$$h = (0.25)(0.683)\left(\frac{(U)(s_s)}{C_1T_g - C_2}\right)^{0.466}\frac{C_3T_g + C_4.}{s_s}. \tag{26}$$

Formulating the convective heat transfer coefficient as a function of T_g allows us to determine $\frac{\partial h}{\partial T_g}$ and estimate the correlation $\overline{h'T'_g}$ using:

$$\overline{h'T'_g} = \frac{\partial h}{\partial T_g}\overline{T'_gT'_g}. \tag{27}$$

Based on the approximated equation for h, we find

$$\frac{\partial h}{\partial T_g} = \frac{(0.25)(0.683)(U)^{0.466}}{ss^{0.534}}\left[\left(\frac{1}{C_1T_g - C_2}\right)^{0.466}C_3 - (0.466)\frac{C_1}{(C_1T_g - C_2)^{1.466}}(C_3T_g + C_4)\right] \tag{28}$$

The correlation between the fluctuations in water evaporation rate and the temperature of the dry fuel, that is $\overline{F'_{H_2O}T'_d}$, is nonzero in the case where the mean dry temperature is above the

temperature for vaporization and there is still additional mass being moved from wet to dry fuel state. In this scenario, a positive fluctuation in the evaporation (as the mean temperature of the wet fuel will always be less than the evaporation temperature) results in the additional mass source for the dry fuel at a temperature lower than the mean dry temperature (a negative temperature fluctuation). If the evaporation rate is non-zero, but the dry temperature has fallen below the temperature for vaporization, we expect a positive fluctuation in the evaporation rate to coincide with a positive fluctuation in the dry temperature. The correlation is expected to increase with the width of the distribution and scale with the mean evaporation rate. Thus, we model this correlation as

$$\overline{F'_{H_2O}T'_d} = -\overline{F_{H_2O}}\sqrt{\overline{T'_dT'_d}}\frac{\overline{T_d}-T_{vap}}{\overline{T_d}}. \tag{29}$$

Equations for Temperature Variance

The evolution of the width of the probability density functions for the temperatures of the wet and dry solids within a volume is tracked based on a similar approach as the development of turbulence transport equations (Daly & Harlow 1970). Similar to velocities and pressure in turbulence modeling, the quantities of equation 16 are decomposed into mean and fluctuating parts. Then, both sides of the equation are multiplied by the fluctuation of the temperature, followed by ensemble averaging of the entire equation. Starting with the dry temperature equation, this process results in the following expression:

$$\begin{aligned} c_{pf}\left(\overline{\rho_d}\overline{T'_d\frac{\partial T'_d}{\partial t}} + \overline{T'_d\rho'_d}\frac{\partial \overline{T_d}}{\partial t} + \overline{T'_d\rho'_d\frac{\partial T'_d}{\partial t}}\right) &= \overline{T'_dq'_d} + \overline{h}\overline{a_{v,d}}\left(\overline{T'_dT'_g} - \overline{T'_dT'_d}\right) \\ &+\overline{hT'_da'_{v,d}}\left(\overline{T_g}-\overline{T_d}\right) + \overline{h}\left(\overline{a'_{v,d}T'_gT'_d} - \overline{a'_{v,d}T'_dT'_d}\right) \\ &+\overline{a_{v,d}}\left(\overline{T'_dh'T_g} + \overline{T'_dh'T'_g} - \overline{T'_dh'T_d} - \overline{T'_dT'_dh'}\right) \\ &+\overline{T'_dh'a'_{v,d}}\left(\overline{T_g}-\overline{T_d}\right) + \overline{T'_dh'a'_{v,d}T'_g} - \overline{T'_dh'a'_{v,d}T'_d} \\ &+\overline{T'_dF'_f}H_f\Theta_d - \overline{F_{H_2O}}\frac{c_{p_f}}{r_{moist,w}}\overline{T'_dT'_d} \\ &+\frac{c_{p_f}}{r_{moist,w}}\overline{F'_{H_2O}T'_d}\left(T_{vap}-\overline{T_d}\right) \\ &-\frac{c_{p_f}}{r_{moist,w}}\overline{F'_{H_2O}T'_dT'_d}. \end{aligned} \tag{30}$$

Rearranging equation 30 and applying the assumptions described above for the mean temperature equations, we arrive at an equation for $\overline{T'_dT'_d}$:

$$\frac{\partial \overline{T'_d T'_d}}{\partial t} = \frac{2}{c_{p_f}\overline{\rho_d}}\left[\overline{q'_d T'_d} + \overline{h}\overline{a_{v,d}}(\overline{T'_d T'_g} - \overline{T'_d T'_d}) + \overline{T'_d F'_f} H_f \Theta_d \right.$$
$$\left. + \frac{c_{p_f}}{r_{moist,w}}\overline{F'_{H_2O} T'_d}\left(T_{vap} - \overline{T_d}\right) - \frac{c_{p_f}}{r_{moist,w}}\overline{F_{H_2O} T'_d T'_d}\right]. \quad (31)$$

Here, we have three unknown terms: $\overline{q'_d T'_d}$, $\overline{T'_d T'_g}$, ; and $\overline{T'_d F'_f}$ that we need to address to close equation 31. The correlation between the evaporation rate and the dry temperature, $\overline{F'_{H_2O} T'_d}$, was discussed in the previous subsection.

For the correlation between radiation and dry temperature, $\overline{q'_d T'_d}$, we assume that the energy absorbed by the fuel particles does not depend on the temperature of the absorbing particles. Thus, the net heat transfer will depend only on the energy emitted from the dry fuel. Leveraging approaches used in variable density turbulence (Besnard et al. 1992) and the Stephan-Boltzmann law for blackbody radiation emission $(q_{emitted} = a_v \epsilon \sigma T^4)$, we can approximate the dependence of a perturbation of the emitted radiation on temperature of the dry fuel with $q'_{emitted} = 4a_v \epsilon \sigma T^3 T'$. . In these equations, σ is the Stephan-Boltzmann constant,ε is emissivity, and we include an added view factor correction, γ, for scenarios where fuel is compacted in the bottom of a computational cell as is the case for litter or grass layer (the value of γ is 1 when the fuel is distributed throughout the cell). This view factor can be thought of as a correction on the area per unit volume. Since emitted radiation is a net negative radiation contribution, this term will act as a sink from the $\overline{T'_d T'_d}$. Furthermore, neglecting a0 terms due to the assumed constant radius of the fuel particle, we arrive at

$$\overline{q' T'_d} = -4\overline{a_{v,d}}\epsilon\gamma\sigma\overline{T_d}^3\overline{T'_d T'_d}. \quad (32)$$

The correlation between temperature of the dry fuel and the reaction rate, $\overline{T'_d F'_f}$, is important in cases where mean temperature is below the combustion temperature but combustion rate might be nonzero, such as instants or locations in which there is a positive temperature fluctuation reaching above the mean temperature. To this effect, positive temperature fluctuations are associated with positive fluctuations in the reaction rate and contribute to the increase in variance of dry temperature, $\overline{T'_d T'_d}$. Similarly, when the mean temperature is greater than the minimum combustion fluctuations can represent locations and instances at which the localized temperature is not sufficient to support the reaction. Thus, there is a negative fluctuation in the reaction rate. However, there are other contributions to the variations in reactions, such as localized mixing and oxygen concentrations, with increasing fraction of the

volume above the critical temperature. Although the correlation, $\overline{T_d' F_f'}$, is expected to be positive, it will decrease with decreasing fraction of the temperature distribution above the critical temperature. This is conceptually shown in Figure 10. Here, we expect the correlation to be closer to zero when $R_{combust}$, which is the fraction of dry fuel that is hot enough to react, is large. However, we anticipate the strongest correlation when less fuel is above the critical temperature ($R_{combust}$ is small). Considering this, we approximate the correlation as

$$\overline{T_d' F_f'} = c_{T_d F} \overline{F_f} \sqrt{\overline{T_d' T_d'}} (1 - R_{combust}) . \tag{33}$$

Where c_{TdF} is taken to be 0.7.

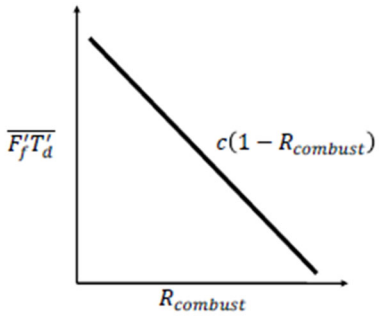

Figure 10: Conceptual plot of the covariance of the reaction rate and dry temperature, $\overline{T_d' F_f'}$, versus the fraction of dry fuel reacting, $R_{combust}$. c is a function of the temperature and the reaction rate.

The final unclosed term in equation 31, $\overline{T_d' T_g'}$, is the correlation between fluctuations in dry fuel temperature and gas temperatures. The correlation between these temperatures is largely related to the rate of convective heat transfer, which lower the temperature difference between adjacent gases and solids. When the convective heat transfer rate is high, perturbations in dry solid temperature are strongly related to the gas temperature perturbations. Since $\overline{T_d' T_g'}$ is symmetric in T_d' and T_g', so should be the modeled term. This covariance is expected to increase depending on the magnitude of the variance of both the dry fuel and gas temperature, as well as the strength of the convection heat transfer. To this end, we propose the following expression for the dry fuel and gas temperature covariance:

$$\overline{h a_{v,d}} \left(\overline{T_d' T_g'} \right) = \overline{h a_{v,d}} \left(1 - e^{-c_h \frac{\bar{h}}{h_{norm}}} \right) \left(\frac{\overline{T_g' T_g'} + \overline{T_d' T_d'}}{2} \right) . \tag{34}$$

In this equation, h_{norm} is the normalization constant for the convective heat transfer coefficient, which is the approximate background value before ignition or heating. In the current study, h_{norm}

is assigned the value of 25.0 $Wm^{-2}K^{-1}$ which is representative of the ambient value of *h* in FIRETEC before fire and during low wind conditions, and c_h = 5. The constant, c_h was determined by comparing modeled fire behavior over a variety of values ranging from 1 to 5 (not shown) for very simple scenarios. We recognize the value for this constant may need to be adjusted in future studies and will be discussed again in later sections.

We now apply the same decomposition and derivation to the instantaneous wet solid temperature equation (equation 13). Thus, taking the ensemble average of the expression yields:

$$\begin{aligned} c_{p_{sw}}\left(\overline{\rho_{sw}}\overline{T'_w\frac{\partial T'_w}{\partial t}}+\overline{T'_w\rho'_{sw}}\frac{\partial \overline{T_w}}{\partial t}+\overline{T'_w\rho'_{sw}\frac{\partial T'_w}{\partial t}}\right) &= \overline{T'_w q'_w}+\overline{h}\,\overline{a_{v,sw}}\left(\overline{T'_w T'_g}-\overline{T'_w T'_w}\right)\\ &+\overline{h}\left(\overline{T'_w a'_{v,sw} T_g}+\overline{T'_w a'_{v,sw} T'_g}\right)\\ &-\overline{h}\left(\overline{T'_w a'_{v,sw}}\,\overline{T_w}+\overline{T'_w a'_{v,sw} T'_w}\right)\\ &+\overline{a_{v,sw}}\left(\overline{T'_w h' T_g}+\overline{T'_w h' T'_g}\right)\\ &-\overline{a_{v,sw}}\left(\overline{T'_w h' T_w}+\overline{T'_w T'_w h'}\right)\\ &+\overline{a'_{v,sw} h' T'_w}\left(\overline{T_g}-\overline{T_w}\right)\\ &+\overline{T'_w h' a'_{v,sw} T'_g}-\overline{T'_w h' a'_{v,sw} T'_w}\\ &+\overline{F'_f T'_w} H_f \Theta_w-\overline{F'_{H_2O} T'_w} H_{H_2O}. \end{aligned} \tag{35}$$

Now, applying analogous simplifications that were discussed previously for the dry fuel equation returns:

$$\begin{aligned} \frac{\partial \overline{T'_w T'_w}}{\partial t} = \frac{2}{c_{p_{sw}}\overline{\rho_{sw}}}\Bigg| &-4\overline{a_{v,sw}}\epsilon\sigma\gamma\overline{T'_w T'_w T_w}^{3}+\overline{h}\,\overline{a_{v,w}}\left(\frac{\overline{T'_g T'_g}+\overline{T'_w T'_w}}{2}\left(1-e^{-\frac{\overline{h}}{h_{norm}}}\right)-\overline{T'_w T'_w}\right).\\ &+\overline{F'_f T'_w} H_f \Theta_w-\overline{F'_{H_2O} T'_w} H_{H_2O}\Bigg|. \end{aligned} \tag{36}$$

Since we assume that the fraction of energy from the combustion process (combustion of dry fuel) deposited on the wet fuel, w, is negligible, the only term left to complete the closure is the covariance of wet fuel temperature and evaporation rate, $\overline{F'_{H_2O} T'_w}$. Using the radiation and convection heat transfer rates, we can formulate the rate at which energy is added to the wet material. When the energy gained by the wet fuels causes the upper limit of the wet fuel distribution to reach or exceed the vaporization temperature (without enforcing the phase change on water or removing the energy of vaporization), evaporation of water begins. The energy available to evaporate water, $\dot{E}_w$, is related to the evaporation rate by $\overline{F_{H_2O}} = \dot{E}_w / H_{H_2O}$. . We define a theoretical ratio for the fraction of wet fuel mass, R_{H2O}, which would have risen

above the evaporation temperature if evaporation had not commenced, assuming the distribution of temperature is symmetric about the mean. Thus, we have:

$$R_{H_2O} = \frac{T_{w_{max}} - T_{vap}}{2C_{pdf}\sqrt{T'_w T'_w}}, \tag{37}$$

where C_{pdf} is a constant with a value as the ratio of halfwidth of the temperature distribution to the standard deviation and T_{wmax} is the maximum temperature in the cell. Moreover, this constant depends on the type of distribution that would be assumed. The mean evaporation rate is therefore determined to be:

$$\frac{\int_{T_{w_{min}}}^{T_{w_{max}}} F_{H_2O}(T)dT}{\int_{T_{w_{min}}}^{T_{w_{max}}} dT} = \overline{F_{H_2O}}. \tag{38}$$

Here, $F_{H2O}(T)$ is the evaporation rate associated with fuel at any specific temperature, T. Now, we define a normalized evaporation rate, F* as:

$$F^*_{H_2O} = \frac{F_{H_2O}(T)}{\overline{F_{H_2O}}}, \tag{39}$$

where

$$F^*_{H_2O} = \begin{cases} 0, & T_{w_{min}} < T < T_{vap} \\ \frac{1}{R_{H_2O}}, & T_{vap} \leqslant T < T_{w_{max}} \end{cases}. \tag{40}$$

This yields unity for the mean normalized vaporization rate:

$$\overline{F^*_{H_2O}} = \frac{\int_{T_{w_{min}}}^{T_{w_{max}}} F^* dT}{\int_{T_{w_{min}}}^{T_{w_{max}}} dT} = \frac{\int_{T_{w_{min}}}^{T_{vap}} 0dT + \int_{T_{vap}}^{T_{w_{max}}} \frac{1}{R_{H_2O}} dT}{2C_{pdf}\sqrt{\overline{T'_w T'_w}}} = 1. \tag{41}$$

Decomposing F^*_{H2O} into its mean and fluctuating components reveals:

$$F^*_{H_2O} = \overline{F^*_{H_2O}} + F^{*'}_{H_2O} = 1 + F^{*'}_{H_2O}. \tag{42}$$

Using these definitions, we can compute $\overline{F'_{H_2O} T'_w}$ as:

$$\overline{F'_{H_2O}T'_w} = \overline{F_{H_2O}}\frac{\int_{T_{wmin}}^{T_{wmax}} F^{*\prime}_{H_2O}T'_w dT}{\int_{T_{wmin}}^{T_{wmax}} dT} = \overline{F_{H_2O}}\frac{\int_{T_{wmin}}^{T_{wmax}} \left(F^*_{H_2O} - 1\right)T'_w dT'}{2C_{pdf}\sqrt{\overline{T'_wT'_w}}} \tag{43}$$

where the temperature range of the wet solid is

$$\overline{T_w} - C_{pdf}\sqrt{\overline{T'_wT'_w}} \leqslant T_w \leqslant \overline{T_w} + C_{pdf}\sqrt{\overline{T'_wT'_w}}. \tag{44}$$

Given the definition of F^*_{H2O}, this simplifies to

$$\overline{F'_{H_2O}T'_w} = \overline{F_{H_2O}}\frac{\int_{T_{vap}-\overline{T_w}}^{C_{pdf}\sqrt{\overline{T'_wT'_w}}} \left(\frac{1}{R_{H_2O}} - 1\right)T'_w dT'}{2C_{pdf}\sqrt{\overline{T'_wT'_w}}}. \tag{45}$$

Using equation 36 in the lower limit of the integral we arrive at:

$$\overline{F'_{H_2O}T'_w} = \overline{F_{H_2O}}\left(\frac{1}{R_{H_2O}} - 1\right)\frac{\left(C_{pdf}\sqrt{\overline{T'_wT'_w}}\right)^2 - \left(C_{pdf}\sqrt{\overline{T'_wT'_w}} - 2R_{H_2O}C_{pdf}\sqrt{\overline{T'_wT'_w}}\right)^2}{4C_{pdf}\sqrt{\overline{T'_wT'_w}}} \tag{46}$$

Manipulating and rearranging these terms, we arrive at:

$$\overline{F'_{H_2O}T'_w} = \overline{F_{H_2O}}C_{pdf}\sqrt{\overline{T'_wT'_w}}\left(1 - R_{H_2O}\right)^2. \tag{47}$$

Final Equations

The following subsection presents a summary of the new model equations with the closure completed for all terms.

$$\frac{\partial\overline{T_d}}{\partial t} = \frac{1}{c_{p_f}\overline{\rho_d}}\left[\overline{q_d} + \overline{h}\overline{a_{v,d}}\overline{T_g} - \overline{h}\overline{a_{v,d}}\overline{T_d} + \frac{\partial h}{\partial T_g}\overline{T'_gT'_g}\overline{a_{v,d}} + \overline{F_f}(H_f\Theta_d)\right.$$
$$\left. + \overline{F_{H_2O}}\frac{c_{p_f}}{r_{moist,w}}\left(T_{vap} - \overline{T_d}\right) + \overline{F_{H_2O}}\frac{c_{p_f}}{r_{moist,w}}\sqrt{\overline{T'_dT'_d}}\frac{\overline{T_d} - T_{vap}}{\overline{T_d}}\right] \tag{48}$$

$$\frac{\partial\overline{T_w}}{\partial t} = \frac{1}{c_{p_{sw}}\overline{\rho_{sw}}}\left[\overline{h}\overline{a_{v,sw}}\overline{T_g} - \overline{h}\overline{a_{v,sw}}\overline{T_w} + \frac{\partial h}{\partial\overline{T_g}}\overline{T'_gT'_g}\overline{a_{v,sw}} - \overline{F_{H_2O}}H_{H_2O}\right] \tag{49}$$

$$\frac{\partial \overline{T'_d T'_d}}{\partial t} = \frac{2}{c_{pf}\overline{\rho_d}}\left[-4\overline{a_{v,d}}\epsilon\sigma\gamma\overline{T_d}^3\overline{T'_d T'_d} + \overline{h}\overline{a_{v,d}}\left(\frac{(\overline{T'_g T'_g} + \overline{T'_d T'_d})}{2}\left(1 - e^{-c_h\frac{\overline{h}}{h_{norm}}}\right) - \overline{T'_d T'_d}\right)\right.$$
$$+c_{T_d F}\overline{F_f}\sqrt{\overline{T'_d T'_d}}\,(1 - R_{combust})\,(H_f \Theta_d) - \overline{F_{H_2O}}\frac{c_{pf}}{r_{moist,w}}\overline{T'_d T'_d}$$
$$\left. +\overline{F_{H_2O}}\frac{\sqrt{\overline{T'_d T'_d}}}{\overline{T_d}}\left(\overline{T_d} - T_{vap}\right)^2\frac{c_{pf}}{r_{moist,w}}\right] \tag{50}$$

and

$$\frac{\partial \overline{T'_w T'_w}}{\partial t} = \frac{2}{c_{p_{sw}}\overline{\rho_{sw}}}\left[-4\overline{a_{v,sw}}\epsilon\sigma\gamma\overline{T_w}^3\overline{T'_w T'_w} + \overline{h}\overline{a_{v,sw}}\left(\frac{\overline{T'_g T'_g} + \overline{T'_w T'_w}}{2}\left(1 - e^{-c_h\frac{\overline{h}}{h_{norm}}}\right) - \overline{T'_w T'_w}\right)\right.$$
$$\left. -\overline{F_{H_2O}}C_{pdf}\sqrt{\overline{T'_w T'_w}}\,(1 - R_{H_2O})^2 H_{H_2O}\right] \tag{51}$$

where $\frac{\partial h}{\partial T_g}$ is described in equation 28.

Proof of Concept Simulations

The new approach described here is intended to capture sub-grid variability in temperatures, and thus increase the generality of wildland fire simulation capabilities. This enables properly simulating high and low-intensity fires. This formulation constitutes the first stage in the development of a multi-phase coupled fire/atmosphere model, which has so far been confined to the solid phase. Since solids are not moving (no advection or spatial diffusion terms), we can study the performance in a single 1m x 1m x 1m control volume where the externally-driven conditions are prescribed, e.g., wind speed, upstream gas temperature, upstream oxygen concentration, and initial fuel moisture. In order to understand the performance of the model described above, we developed a series of idealized tests by varying initial fuel moisture conditions, wind speeds, and upstream gas temperatures. The wet fuels (fuels at their initial moisture state) are assumed to have an initial bulk density of 0.5 kg m^{-3} and moisture fractions of (a) 0.05; (b) 1; and (c) 2. These correspond to fuel conditions similar to (a) dry dead needles and fine branchwood or matted dead grass; (b) live conifer fine branchwood and needles; and (c) live deciduous fine branchwood and leaves, respectively. Wind speeds have constant values of 0.1 m s^{-1}, 1 m s^{-1} and 2 m s^{-1} as this is a plausible set of wind speeds very near the ground (height below 1 m) in the vicinity of a surface fire. For a special case, we apply a wind speed value of 4 m s^{-1}, which constitutes a high-intensity fire. For the purposes of this paper, wildfire intensity is

assumed to range from low-intensity fires that have depths and flame lengths 10s of cm up to intense fires that have burning zones of 10s of meters and flame lengths of similar size.

Even though the focus of these proof of concept simulations is modeling the solid phase temperatures and their variations, it is necessary to vary the local gas temperature for the closure of the convective heat transfer terms. For this purpose, a simplified evolution equation is developed that combines the prescribed velocity and upwind temperature, the convective heat transfer coefficient, an area per unit volume, and a grossly simplified radiation energy sink. This expression estimates the gas temperature in the control volume:

$$c_{v_{air}} \rho_g \frac{\partial \overline{T_g}}{\partial t} = \overline{q_g} + c_{v_{air}} \rho_g U \frac{\partial \overline{T_g}}{\partial x} + h a_{v,d} \left(\overline{T_d} - \overline{T_g} \right) + h a_{v,sw} \left(\overline{T_w} - \overline{T_g} \right) + \overline{F_f} H_f \Theta_g \tag{52}$$

Here, c_{vair} is 718 J kg^{-1} K^{-1}, $q_g = -\frac{O_{2_{ambient}} - O_2}{O_{2_{ambient}}} \sigma \overline{T_g}^4$, which is the radiation loss scaled by the oxygen depletion that relates gas emissivity combustion products in oxygen poor environment, and g is 0.75 (75% of reaction energy deposited in gas and 25% in the solid), which is the fraction of reaction energy absorbed by the gas phase. This equation for the gas temperature is simply intended to capture the fact that there is feedback between the solid and gas temperatures and the influences of energy in surrounding regions on gas temperatures.

The variance of gas temperatures is prescribed based on the mean gas temperature using the following equations. This first equation,

$$\overline{T_g' T_g'} = \left(30 + \frac{\overline{T_g} - 243.59}{3} \right)^2 \tag{53}$$

is the variance assigned to the low-intensity gas scenario, which ensures that the minimum gas temperature in the assumed wide distribution does not fall below 300 K. The second version of the prescribed gas variance is:

$$\overline{T_g' T_g'} = \left(60 + \frac{\overline{T_g} - 300}{6} \right)^2 \tag{54}$$

which we assigned for the other simulations. In subsequent phases of this study, related to the development of a multi-phase sub-grid fire-atmosphere model, these gas temperature equations are replaced with full transport equations, similar to the technique applied for the solid phase in the current study.

Initially, the gas temperatures in the control volume in all of the idealized simulations were assumed to be 300 K, before upwind gases began to advect into the control volume. High-

intensity fire scenarios were simulated by assigning an upwind mean gas temperature that starts at 300 K, and ramps up to 1000 K over 15 seconds and tapers off following this relation:

$$\overline{T_{g_{uw}}} = 300 + \frac{700}{2}\left(0.95 - 0.95\tanh\left(\frac{t-15}{50}\right) + 0.05\right), \tag{55}$$

and the low-intensity fires were simulated with the upwind temperatures rising from 300 K to 500 K over 100 s and tapers off as :

$$\overline{T_{g_{uw}}} = 300 + \frac{200}{2}\left(0.95 - 0.95\tanh\left(\frac{t-500}{120}\right) + 0.05\right). \tag{56}$$

Additionally, we prescribe an oscillating upwind gas temperature with the following equation:

$$\overline{T_{g_{uw}}} = 750 + 450\sin\left(\frac{(t-15)2\pi}{60}\right). \tag{57}$$

All three upwind gas temperature prescriptions for the idealized scenarios are plotted in Figure 11.

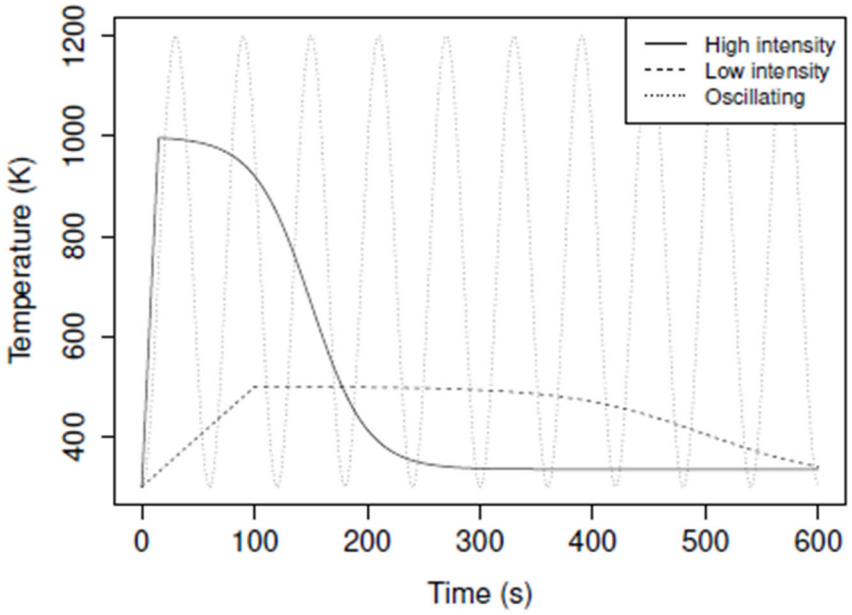

Figure 11: Prescribed upwind gas temperature over time for the high-intensity, low-intensity, and oscillating scenarios.

The first two temperature scenarios, involving near-sustained elevated gas temperatures, were designed to reduce the complexity of environmental drivers with the elevated temperature that represent gases advected from upwind with the approaching fire. The third gas temperature

paradigm was chosen specifically to highlight the response of the model in dynamic environments with oscillating conditions. It was assumed that the high-intensity spreading fire scenarios were unlikely to coincide with light winds and thus we used only the case of wind speed at 4 m s^{-1} and temperature of 1000 K. The time step for all simulations is 0.001 s and we temporally discretize the differential equations using an explicit forward-in-time Euler method. The simulations ran for at least 600 s.

The size scale of the fuel (half of the volume to surface area ratio) remains constant and is prescribed as 0.0006 m, which corresponds to roughly that of thermally thin grass, needles, or fine branchwood. Thermally thin fuel refers to fine fuel particles that are assumed to have no internal temperature gradients. As such, an individual fuel particle will warm and cool uniformly. Non-thermally thin fuel particles will be addressed in future efforts, which would build on some approaches that have been outlined in this document.

Sub-grid turbulent kinetic energy (TKE) is fixed at k_a = 0:125U^2, k_b = 0:005U^2 and k_c = 0:2k_b m^2 s^{-2}, where U is the prescribed scalar wind speed. FIRETEC incorporates three subgrid TKE scales (and their associated turbulence energy spectra) corresponding roughly to the unresolved scales associated with vegetation structure. Additional information on sub-grid TKE in FIRETEC is discussed by Linn (1997). For the purposes of this concept demonstration, the turbulent length scales are equivalent to the distance between larger vegetation structures (e.g., shrubs), branches, and needles.

The radiation loss terms are computed using the mean and variance of the wet and dry fuel temperatures to compute T^4 and blackbody radiation. The effective area that radiates energy away from the solid is estimated based on the surface area per unit volume times γ, which is the ratio of the fuel depth height to cell height (a compression factor):

$$q = \gamma a_v \epsilon \sigma \overline{T^4}. \tag{58}$$

While radiation ahead of the flame front has a role in preheating fuels, radiation alone does not typically induce fire spread in fine wildland fuels that are loosely packed due to attenuation in low-density discontinuous fuels, and the fact that convective cooling between fine fuel elements counteracts radiative heating, as was discussed by Finney et al. (2015). Results from their experiments provide strong evidence that convection is largely responsible for wildland fire spread (Cohen & Finney 2022b,a). Thus, in the interest of simplicity, we omit the influences of radiative heating in this initial testing phase. The radiative heating will be addressed in more detail in subsequent efforts.

The evaporation rate is calculated by first determining the difference between the energy gained by the wet fuel through convective and radiative heat transfer within one time step and the energy that it takes to raise the temperature distribution to the point where the max temperature reaches 373 K. This residual energy is the energy available to evaporate water within the time step and determine the water evaporation rate. The theoretical maximum temperature,

T^*_{wmax}, that would be reached within a time step without accounting for the phase change provides an estimate for the fraction of fuel, R_{H2O}, that would be above 373 K due to the radiative and convective heating and cooling. For this initial effort, we use a top hat distribution. Using this simplified distribution, $C_{pdf} = \sqrt{3}$ in equation 36. We recognize that if a normal distribution is applied instead, R_{H2O} is a form of the error function. We will be exploring this topic in the future, separately.

We apply a similar philosophy to determine what fraction of the fuel in a cell is above the critical temperature for combustion, ψ . This fraction is used in the mixing limited reaction rate as described by Linn (1997).

A simplified model for the advection and consumption of oxygen density is used to represent the depletion and replenishment of oxygen with time. The available oxygen is initialized as 21% of the air density, and over time it is calculated explicitly using the following equation:

$$\frac{\partial O_2}{\partial t} = -F_f N_{oxygen} - U\frac{\partial O_2}{\partial x}. \tag{59}$$

Here, N_{oxygen} is the stoichometric coefficient for oxygen in the combustion reaction (Drysdale 1985) normalized by the total mass of reactants. The upwind oxygen value is related to the upwind temperature, such that as temperature decreases/increases oxygen increases/decreases proportionally between ambient, 0:21$\rho_{gambient}$, and 0.15 kg m^{-3}. Corresponding to the upwind drop in temperature, we assign upwind oxygen, such that:

$$\overline{O_{2_{uw}}} = 0.15 + \frac{0.09}{2}\left(0.95 - 0.95\tanh\left(-\frac{t-15}{50}\right) + 0.05\right) \tag{60}$$

in the high-intensity simulations, and

$$\overline{O_{2_{uw}}} = 0.15 + \frac{0.09}{2}\left(0.95 - 0.95\tanh\left(-\frac{t-500}{120}\right) + 0.05\right) \tag{61}$$

for the low-intensity cases. Lastly, the upwind oxygen concentration in the oscillating simulations is

$$\overline{O_{2_{uw}}} = 0.18 - 0.06\sin\left(\frac{(t-15)2\pi}{60}\right). \tag{62}$$

All three scenarios are plotted in Figure 12.

Finally, we only apply the equations for temperature of the wet/dry fuel equations and their variances when their respective density is greater than 1x10^{-6} kg m^{-3}. We also assume that the fraction of energy deposited directly back onto the fuel, Θ_d, is 0.25.

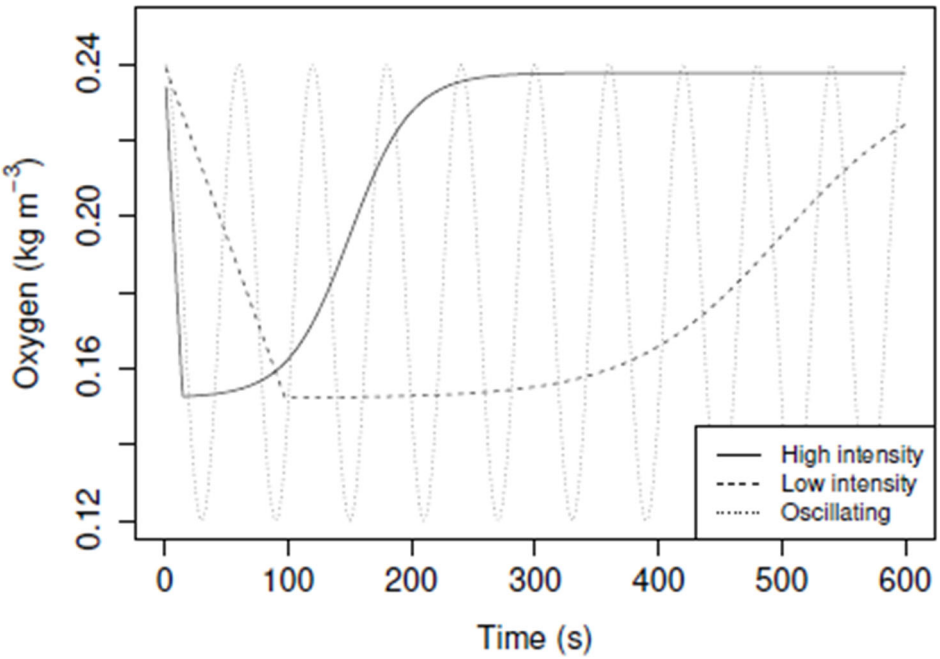

Figure 12: Upwind oxygen concentrations where changes are inversely proportional to temperature changes.

Proof of Concept Simulation Results

We begin with scenarios of high-intensity fire placed upwind of the control volume. We simulate high upwind temperature with high wind speed for all local moisture scenarios shown in Figure 13 and Table 1. In these simulations, the mean upwind gas temperature is raised from 300 K to 1000 K over 15 s with a slow decline back to ambient temperature. It is unlikely that a 1000 K gas temperature would coincide with light winds. Thus for this high-intensity simulation, we present the results for only the case of 4 m s^{-1} wind speed, applied to all three fuel moisture scenarios (5%, 100% and 200%).

In these Figures, mean wet and dry fuel temperatures are only shown in cases with the density above $1x10^{-6}$kg m^{-3}. The blue solid line with circles indicates the mean wet fuel temperature, the red line with squares is the mean dry fuel temperature, the light grey line is the mean gas temperature, the solid purple line is the upwind prescribed gas temperature, and the dashed blue and dotted red lines are the wet fuel and dry fuel density, respectively. Shading corresponds to one standard deviation above and below the mean temperature value.

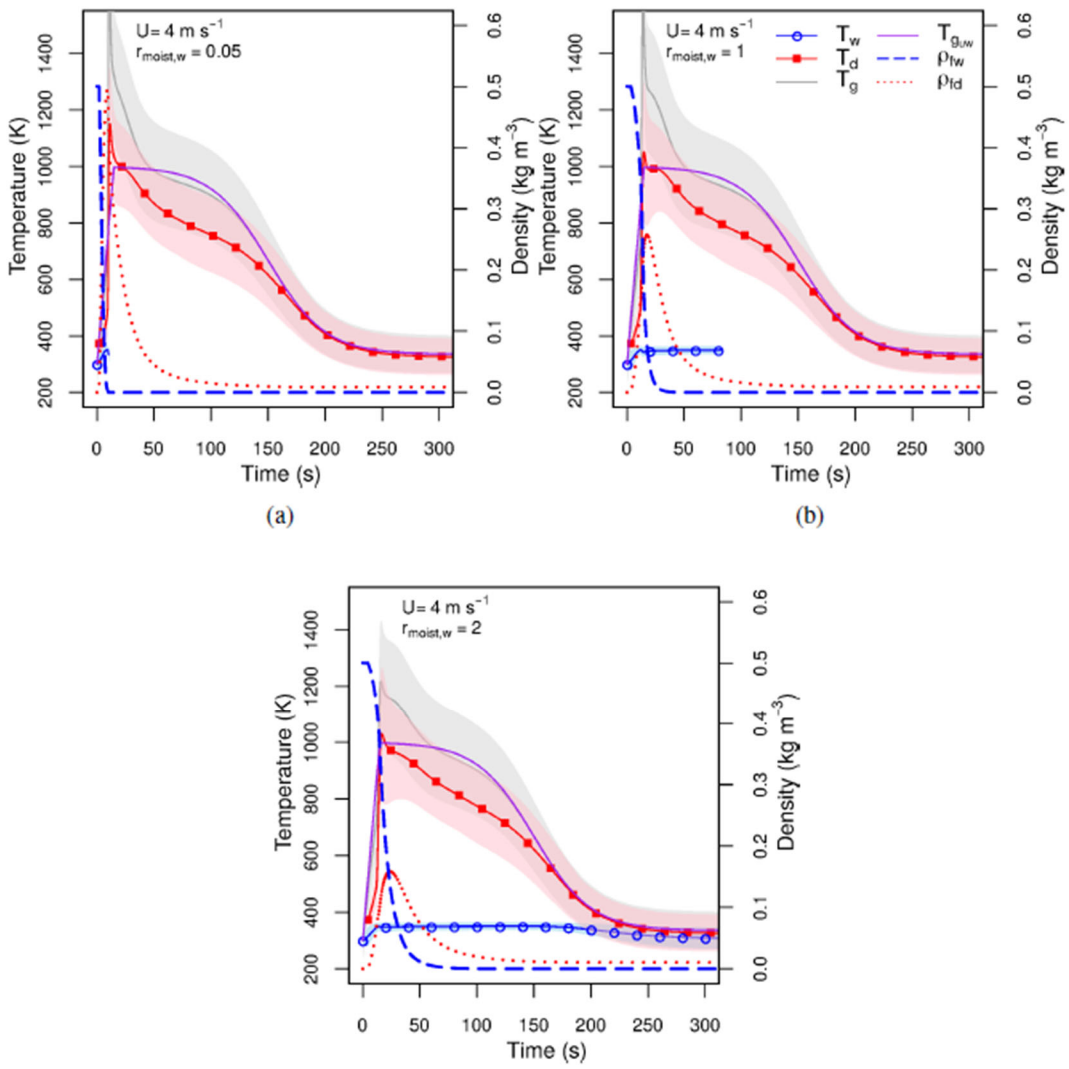

Figure 13: Model results for high intensity fire with 4 m s^{-1} winds at a) moisture fraction 0.05, b) moisture fraction 1 and c) moisture fraction 2. Temperature is plotted only when the respective fuel density is above $1x10^{-6}$ kg m^{-3} and shading indicates 1 standard deviation above and below the mean temperatures.

U	$r_{moist,w}$	t_{e_0}	te_f	t_{c0}	ρ_{d_c}	T_{max}	tT_{max}	t_{f50}	t_{f75}	$\rho_{d_{600}}$
4.0	0.05	2	10	9	0.494	1151	11	17.6	29	0.009
4.0	1.00	3	82	12	0.134	1052	15	22.6	34	0.009
4.0	2.00	5	-	12	0.065	1030	17	27.5	42	0.010

Table 1: 1000 K gas temperature simulation results under wind [U (m s^{-1})], and moisture fraction [$r_{moist,w}$] scenarios for evaporation initiation time [t_{e_0} (s)], evaporation completion [t_{e_f} (s)], combustion initiation [t_{c_0} (s)], density of dry fuel at combustion initiation [ρ_{d_c}(kg m^{-3})], the peak temperature [$T_{max}(K)$], the time of peak temperature [tT_{max} (s)], the time for 50% [t_{f50} (s)] and 75% [t_{f75} (s)] fuel consumption, and the density at 600 s [$\rho_{d_{600}}$(kg m^{-3})].

In all moisture fraction scenarios, a fraction of wet fuel is quickly dried and dry fuel begins to burn within the first 12 seconds of all simulations. It should be noted that there is an assumption that there are burning ashes etc. present, such that ignition is piloted. At the onset of combustion in the fuel with moisture fraction of 0.05, 99% of the fuel is already dried (i.e., 99% moved from the wet to dry fuel category) and thus available for consumption. This can be contrasted to 27% and 13% of the fuels that have been dried when combustion starts for the fuels with moisture fractions 1 and 2, respectively. The maximum temperature is slightly higher in the lower moisture fraction scenarios, but the time for the peak temperature differs only by 5 seconds amongst these three simulations. The similarity between these three cases is indicative of the fact that the strong winds and high temperatures are very significant and they overwhelm the effects of moisture on combustion initiation. It is important to remember that the prescribed high-intensity conditions are associated with fire upwind of the control volume, likely indicating abundance of dry fuel in that region. The similarity of the results relates to the fact that when a fire moves from one set of conditions to a new set of conditions, the changes to fire behavior do not occur instantaneously (time or space). Thus when our control volume has high moisture (i.e. moisture ratio, or fractions, of 1 or 2), the high-intensity fire from upstream still ignites the fuel and consumes it, but the energy release (proportional to the dry mass loss rate) is lower in the wetter fuel cases. We also note that the temperature begins to decrease after the initial reaction in all scenarios, as a combined result of reduced oxygen availability leading to lower reaction rates and convective cooling. After 600 s, only 2.1% or less of the fuel remains in all simulations, which indicates near complete fuel consumption regardless of moisture content. This is consistent with observations and empirical models in a high-intensity wildfire. During high-intensity crown fire, where observed in-fire mean gas temperatures exceed 1000 K (e.g., Taylor et al. 2004), the fraction of fine fuels (less than 5 mm diameter) that are consumed is high and often approaches 100% (Forestry Canada Fire Danger Group 1992; Call & Albini 1997; Stocks et al. 2004; Thompson et al. 2020; de Groot et al. 2022).

Reducing the upwind gas temperature and variance after 100 s provides enough time to examine the fire behavior simulated in the model at constant high intensity. For all simulations presented here, it is important to remember that holding the wind and upwind gas temperature steady (and remaining steady for an extended period of time) is unrealistic. However, doing so allows us to observe the model behavior without the extremely complex influence of varying wind and gas temperatures on the fire behavior.

Evaluating the results in Figure 14 and Table 2, we next examine the behavior of our proposed model for a lower-intensity upwind fire scenario and a lower-mean upwind gas temperature with a higher variance. These conditions are selected to illustrate the behavior of the proposed model during a low-intensity head fire impinging on a cell, or flanking/backing fire behavior where only a fraction of the gas temperature within the cell would be hot enough to initiate combustion in the dry fuel. In these scenarios, the upwind gas temperature begins at ambient, ramping up to 500 K over 100 seconds and slowly decreasing as shown in Figures 11 and 14. The results presented in Figures 14a - 14c correspond to wind speed 0.1 m s^{-1}, Figures 14d - 14f to wind speed of 1.0 m s^{-1}, and Figures 14g - 14i to a wind speed of 2.0 m s^{-1}. Furthermore, Figures 14a, 14d, and 14g correspond to moisture fraction of 0.05, Figures 14b, 14e and 14h are moisture fraction of 1, and Figures 14c, 14f and 14i show results for moisture fraction of 2.

U	$r_{moist,w}$	t_{e0}	t_{ef}	t_{c0}	ρ_{d_c}	T_{max}	$t_{T_{max}}$	t_{f50}	t_{f15}	$\rho_{d_{600}}$
0.1	0.05	23	209	-	-	375	155	-	-	0.5
0.1	1.00	38	-	-	-	373	0	-	-	0.5
0.1	2.00	50	-	-	-	373	0	-	-	0.5
1.0	0.05	10	95	114	0.5	858	1251	147	192	0.051
1.0	1.00	17	-	-	-	430	239	-	-	0.5
1.0	2.00	23	-	-	-	427	276	-	-	0.5
2.0	0.05	7	81	95	0.5	929	102	1156	142	0.030
2.0	1.00	14	524	111	0.348	914	119	131	161	0.033
2.0	2.00	19	-	133	0.276	921	141	156	206	0.043

Table 2: 500K gas temperature for each wind and moisture scenario. The columns are the same as described in Table 1. The Table is organized consecutively corresponding to Figure14subfigures a)-i)

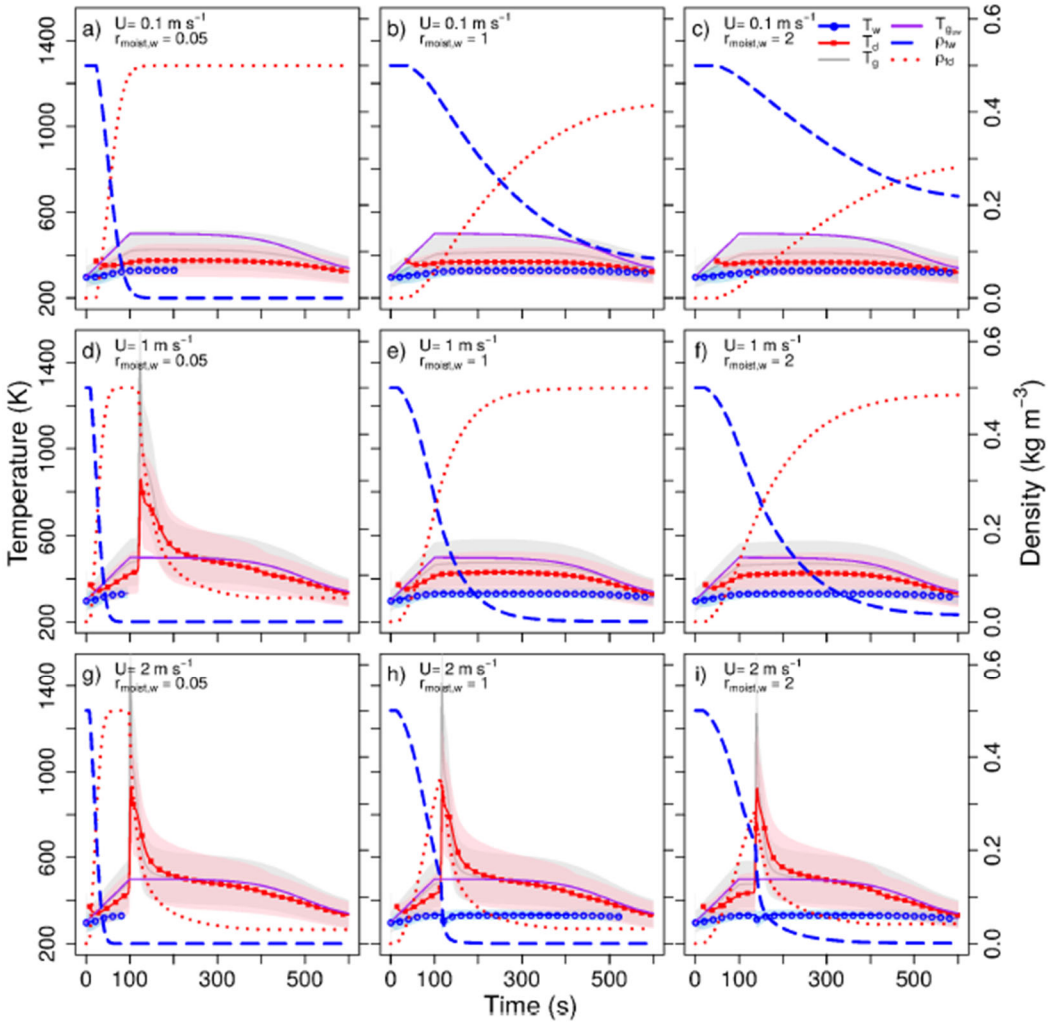

Figure 14: Results for wind speed and moisture fractions applied to the low intensity gas scenario.

In simulations where the wind speed is near calm (Figures 14a-14c), convective heat transfer is not significant enough to warm the fuel and overcome radiative losses. Thus, no fraction of the fuel is warm enough to begin combustion in any of the scenarios. Increasing the wind speed to 1 m s^{-1} provides enough convective heating to induce combustion when the fuel is dry. However, the energy sink required to evaporate water from the fuel with a higher moisture content prevents combustion from occurring. Increasing the wind speed to 2 m s^{-1} results in all moisture scenarios reaching the threshold for combustion. Interestingly, the fuel consumption in all cases where combustion occurs is 90% or greater. This result is somewhat surprising since during a low-intensity burn we would expect less than 90% consumption. For these idealized cases with constant winds and steady gas temperature prescription, however, we are not capturing the effects of cool air entertainment. This can contribute to residual unburned fuel. Furthermore, the elevated upwind temperatures persist for more than 5 minutes, which is likely unrealistic over a

1 m spatial scale in some of these scenarios. Arguably, a near surface wind speed of 2 m s^{-1} would produce a higher intensity surface fire than we are prescribing upwind, especially for the driest fuel. For example, the Canadian Forest Fire Behavior Prediction system (Forestry Canada Fire Danger Group 1992), an empirically-based system used by fire management agencies, predicts a moderately intense fire with 1.3 m s^{-1} forward rate of spread in dead matted grass that has a moisture content of 5% if we estimate the 10 m open wind speed to be 5.4 m s^{-1} using a simple logarithmic wind profile with 2 m s^{-1} wind at 1 m, roughness length z = 0:05m and zero plane displacement d = 0:65m. Considering the depth of the fireline (being at most tens of meters deep) and the forward rate of spread, the residence time for such a fire would be much less than 5 minutes (Cheney and Sullivan 2008; Wotton et al. 2012) in this case.

In simulations where wet fuel is still being converted to dry fuel during combustion (Figures 14h and 14i), the initiation of burning coincides with a slight decrease in mean wet fuel temperature. Since the mass of wet fuel drops quickly in response to accelerated evaporation caused by the increase in gas temperature, the mean temperature of the wet fuel will fall as the warmest of the wet fuel is converted to dry fuel and the cooler of the wet fuel remains. Furthermore, the sharp increase in temperature at the onset of combustion is more rapid than expected for a low-intensity scenario in a cell 1m x 1m and is due to the fact that 1) we do not simulate cool air entertainment and temperature fluctuations from surrounding cells when the upwind gas is elevated (as already discussed), and 2) we may not be accurately capturing the oxygen concentration in the control volume. This also likely contributes to a larger fraction of fuel being consumed than is expected during marginal conditions. These limitations will be corrected with coupling of the gas equations to the fuel equations in the near future, where we capture the influence of adjacent cells (i.e., more realistic advection of gas and oxygen) and turbulent variations.

The main motivation behind this work is to improve the sub-grid models for fire behavior simulations through the development of new closure schemes. Thus, we proceed with examining the individual terms and closures in the proposed model, specifically looking at the processes in Figure 5i. This simulation was selected since it highlights the most important processes in the lower-intensity upwind scenarios, i.e., slower warming and evaporation, moderate wind speeds, higher moisture, and eventual but delayed combustion. Hereafter, we represent all terms in Figure 6 related to radiation contribution as α_x, all terms related to convection as β_x, all terms related to the heat of combustion or heat of vaporization as δ_x, and all other terms as ε, where x denotes d for the mean dry fuel temperature, dv is the mean dry fuel temperature variance, w is the mean wet fuel temperature, and wv is the mean wet fuel temperature variance. In the case where β_x or ε_x have two terms, these terms are assigned in the order that they are shown in the governing equations that have been outlined in previous sections. These terms are more specifically outlined in Table 3.

Wet fuel terms contributing to the mean and variance of temperature

α_w	$\overline{q_w}$	α_{wv}	$-4\overline{a_{v,w}}\epsilon\sigma\gamma\overline{T_w}^3\overline{T_w'T_w'}$
β_w	$\overline{ha_{v,sw}}(\overline{T_g}-\overline{T_w})$	β_{wv}	$\overline{ha_{v,sw}}\left(\frac{\overline{T_g'T_g'}+\overline{T_w'T_w'}}{2}\left(1-e^{\frac{\overline{h}}{h_{norm}}}\right)-\overline{T_w'T_w'}\right)$
β_{w2}	$\overline{a_{v,sw}}\frac{\partial h}{\partial T_g}\overline{T_g'T_g'}$	β_{wv2}	-
δ_w	$-\overline{F_{H_2O}}H_{H_2O}$	δ_{wv}	$-\overline{F_{H_2O}}C_{pdf}\sqrt{\overline{T_w'T_w'}}\,(1-R_{H_2O})^2\,H_{H_2O}$
ϵ_w	-	ϵ_{wv}	-
$\epsilon_w 2$	-	ϵ_{wv2}	-

Dry fuel terms contributing to the mean and variance of temperature

α_d	$\overline{q_d}$	α_{dv}	$-4\overline{a_{v,d}}\epsilon\sigma\gamma\overline{T_d}^3\overline{T_d'T_d'}$
β_d	$\overline{ha_{v,d}}(\overline{T_g}-\overline{T_d})$	β_{dv}	$\overline{ha_{v,d}}\left(\frac{(\overline{T_g'T_g'}+\overline{T_d'T_d'})}{2}\left(1-e^{-\frac{\overline{h}}{h_{norm}}}\right)-\overline{T_d'T_d'}\right)$
β_{d2}	$\overline{a_{v,d}}\frac{\partial h}{\partial T_g}\overline{T_g'T_g'}$	β_{dv2}	-
δ_d	$\overline{F_f}H_f\Theta_d$	δ_{dv}	$\overline{F_f}\sqrt{\overline{T_d'T_d'}}(1-R_{combust})\,H_f\Theta_d$
ϵ_d	$\overline{F_{H_2O}}\frac{c_{p_f}}{r_{moist,w}}\left(T_{vap}-\overline{T_d}\right)$	ϵ_{dv}	$-\overline{F_{H_2O}}\frac{c_{p_f}}{r_{moist,w}}\overline{T_d'T_d'}$
ϵ_{d2}	$\overline{F_{H_2O}}\frac{c_{p_f}}{r_{moist,w}}\sqrt{\overline{T_d'T_d'}}\frac{\overline{T_d}-T_{vap}}{\overline{T_d}}$	ϵ_{dv2}	$\overline{F_{H_2O}}\frac{\sqrt{\overline{T_d'T_d'}}}{\overline{T_d}}\left(\overline{T_d}-T_{vap}\right)^2\frac{c_{p_f}}{r_{moist,w}}$

Table 3: Terms and abbreviated symbols for Figure 15.

Beginning with the solid wet fuel mean temperature and variance, as shown in Figures 15a and 15b, the mean temperature rises and the variance increase in response to increasing gas temperature at the onset of the simulation. This is via convection before the onset of evaporation at 19 s. Once evaporation begins, convection source terms, β_w and β_{wv}, and the sinks associated with heat of evaporation, δ_w and δ_{wv}, increase the mean temperature and reduce the variance respectively, as warm wet fuel is being converted to dry fuel. Regarding the dry temperature results in Figure 6c, the mean dry fuel temperature falls with the radiative and convective cooling sinks, α_d and β_d, exceeding the source of warm dry fuel, d, until the gas temperature rises above the mean dry temperature. This results in positive convective heat transfer, which forces a rise in dry temperature. At the same time, we observe a rise in the variance (Figure 15d) of the dry fuel, since the positive contribution from the convective term, β_{dv}, outweighs the sink from radiation, and the dry fuel mass source terms, α_{dv} and ε_{dv}, respectively (Figure 15 d).

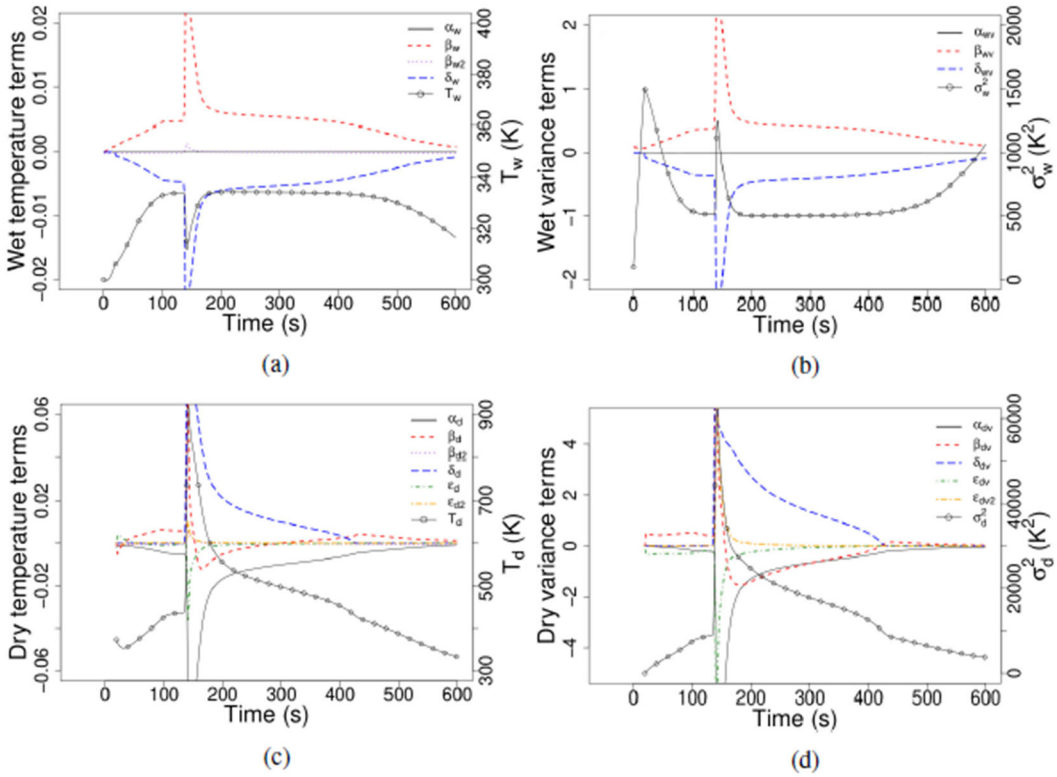

Figure 15: Individual term contributions averaged over 1 s for a) the dry fuel temperature equation, b) the dry fuel variance equation, c) the wet fuel temperature equation and d) the wet fuel variance equation in the wind 2 m s^{-1}, fuel moisture fraction 2 and gas temperature 500 K scenario. The terms in the legend appear as ordered in the derived equations and are discussed further in Table 3. All terms shown are multiplied by $\frac{\Delta t}{c_p \rho}$ or $\frac{2\Delta t}{c_p \rho}$ for the corresponding specific heat capacity and density.

The dry variance and mean temperature continue to rise until a fraction of mass in the dry fuel temperature distribution reaches 600 K (at approximately 133 s) and pyrolysis / combustion begins. The exothermic reaction source term, δ_d, quickly raises the mean temperature of the dry fuel. This is while the combined sources, δ_{dv}, β_{dv} and ε_{dv2}, are greater than the combined sinks, α_{dv} and ε_{dv}. This results in a rapid net increase of the variance. As previously discussed for the onset of combustion, we observe energy and mass losses in the wet fuel, which are due to rapid heating. Thus, the sudden drop in δ_w results in a momentary decrease of the mean wet fuel temperature and an increase in the wet fuel variance as warm wet fuel is quickly converted to dry fuel.

The mass loss due to combustion coincides with depleted oxygen and lowering of the reaction rate, δ_d. This, combined with convective cooling and mass gain at lower temperatures (β_d and ε_d), leads to a drop in mean temperature. Similarly, δ_{dv} in the variance equation falls as the reaction rate drops the resulting source term. This combined with the sinks related to radiation, α_{dv}, and cooling (convective and mass gain, β_{dv} and ε_{dv}) the variance falls as well. At this stage, the upwind prescribed gas temperature is decreasing and all source and sink terms are reduced in all equations until both the reaction and evaporation cease, and convection and radiation are the only contributing terms.

The qualitative examination of the individual terms in the reaction for low mean gas temperatures with high variance provides a reasonable explanation for the observed fire behavior in the conceptual model presented here. Most of the known processes are represented in this simple scenario and the equations are well behaved. Although we are unable to directly compare the results of this study with observed in-fire data to determine the accuracy of magnitude and relative contributions of the individual terms, the net fire behavior follows the expected trends. We acknowledge the scenarios presented are unrealistic given constant or steady wind, mean upwind gas temperatures, and gas variance. However, we are able to examine the behavior of the model by removing the complexities of variations in gas temperature and wind speed due to turbulence. This also enables examining the impact of each of the terms and closures presented here.

The final set of idealized gas scenarios presented is driven by an oscillating upwind gas temperature, which alternates between 300 and 1200 K with a 60 s period as shown in Figure 16 and Table 4. Wind and moisture are the same as outlined in Figure 15. In all simulations, we observe a step-like structure in the density as a response to the fluctuations in gas temperature. As gas temperature increases, the movement of mass from wet to dry accelerates, and its decrease coincides with slowing of the mass transfer. Moreover, this step-like structure is evident in the mass decrease of dry fuel as well, particularly in the two higher wind speed scenarios, in which convective heat transfer and mixing are stronger.

All simulations achieve combustion, except the highest moisture fraction with the lowest wind speed. Interestingly, the fuel consumption in the lowest wind scenario is significantly lower than all other simulations presented, with 20% and 49% of the fuel remaining at 600 s in the 0.05 and 1 moisture fraction, respectively. This is compared to 1.1% to 1.9% remaining in the same moisture scenarios when the winds are stronger.

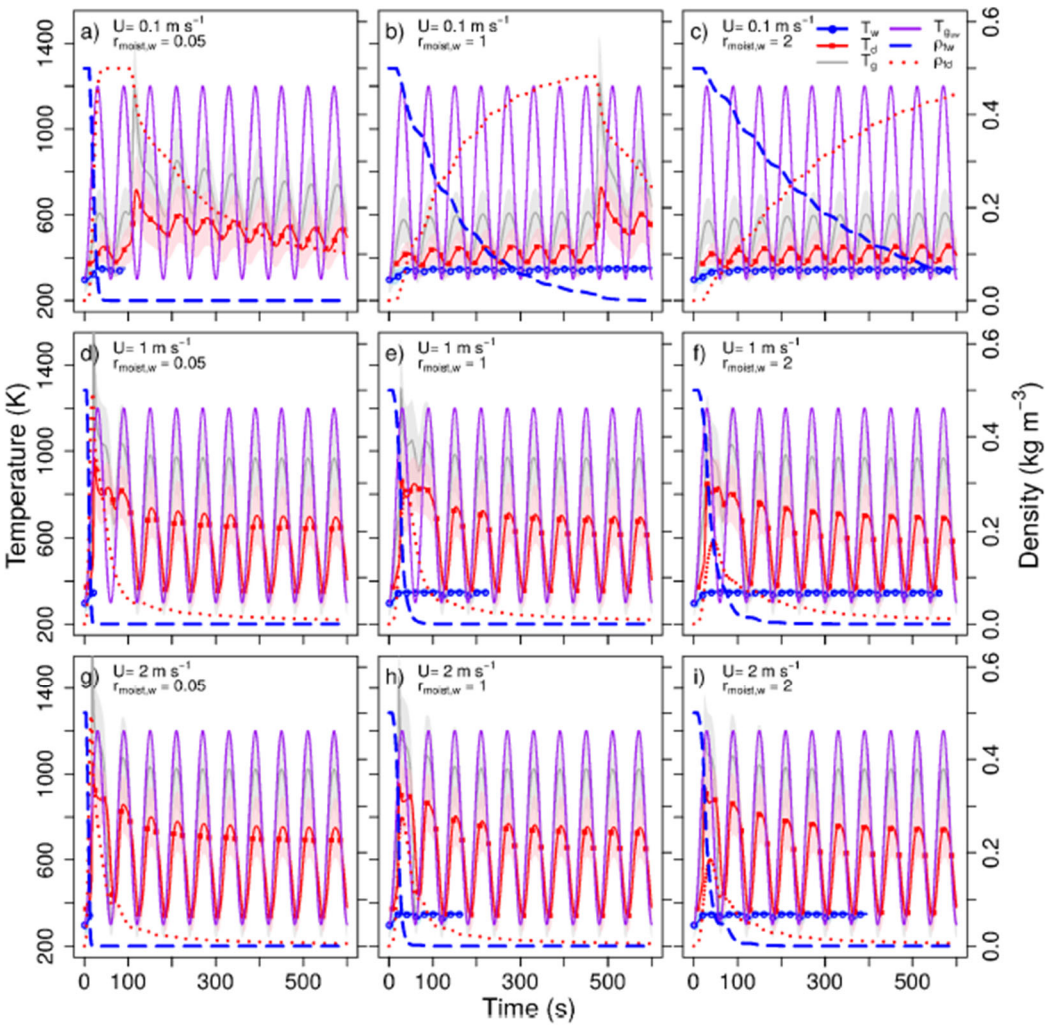

Figure 16: Wind speed and fuel density scenarios for gas temperature oscillating between 1200 K and 300 K with a 60 s period. The wind and moisture scenarios are the same as described in Figure 13.

U	$r_{moist,w}$	t_{e0}	t_{ef}	t_{c0}	ρ_{d_c}	T_{max}	$t_{T_{max}}$	t_{f50}	t_{f75}	$\rho_{d_{600}}$
0.1	0.05	11	92	99	0.5	718	118	232	463	0.100
0.1	1.00	17	-	460	0.485	728	485	595	-	0.245
0.1	2.00	21	-	-	-	455	5838	-	-	0.5
1.0	0.05	5	22	18	0.495	968	23	45	66	0.009
1.0	1.00	8	273	23	0.138	866	29	52	72	0.009
1.0	2.00	11	591	23	0.068	856	32	59	91	0.011
2.0	0.05	4	18	16	0.495	1053	19	32	51	0.006
2.0	1.00	7	203	19	0.135	955	24	40	56	0.006
2.0	2.00	9	411	19	0.065	942	26	45	82	0.006

Table 4: Oscillating gas temperature for each wind and moisture scenario.The columns are the same as described in Table 1.

We observe a rapid rise in dry temperature at the onset of combustion in the higher wind speed simulations (Figures 16d-16i), similar to the two previous gas scenarios discussed earlier. However in the lower wind speed scenario with a slower fuel response time due to reduced convective heat transfer (Figures 16a-16b), we observe a markedly cooler peak temperature with a slower decline. Because of this slower response time, when combustion finally occurs, the upwind temperature is already in the decreasing phase of the oscillation and so the control volume and upwind gas temperature is cooler at the onset of combustion (compared to the previous scenarios). This leads to a slowed acceleration and deceleration of the reaction rate and a lower overall maximum temperature. This phase could loosely be compared to the effects of cool air advection from surrounding cells and turbulence/vorticity-induced cooling. As discussed by Finney et al. (2015), local temperatures fluctuate rapidly as a result of the effects of turbulence and buoyancy-induced circulation, which can be periodic in both stream-wise and transverse directions. Since we are not incorporating these effects in the control volume boundary conditions, it is reasonable to assume that we can expect variation in reaction rate and mean dry fuel temperature when coupling the unsteady gas equation and fuel equations in three-dimensional scenarios. Future work that includes more accurate oxygen advection should further improve the reaction and fuel consumption rates.

In these simulations, the lag and offset between the dry fuel temperature, the cell level gas temperature, and the upwind gas temperature is most pronounced in the low wind scenario for all three moisture fractions. This is due to the reduced convective energy transfer for solid-to-gas and gas-to-solid. The variations in wet fuel temperature in response to variations in gas temperature similarly increase with wind speed. Unlike the low-intensity scenario shown in Figure 5, we observe a very modest decrease in wet fuel temperature during the onset of combustion. Instead, changes in wet fuel temperature are mainly a result of gas temperature variation in the control volume.

Effects of Gas Temperature Variance on Dry Fuel

While we only present the results for a single control volume whose fuel evolution is not directly dependent on cell size (although the overly simplified gas temperature and oxygen equation assume a 1 m upwind distance), the improvement of sub-grid temperature distribution relaxes the current restraint on cell size in three-dimensional formulations of FIRETEC. The proposed model for the evolution of sub-grid temperature distribution is expected to improve the current static shape of sub-grid temperature distribution in FIRETEC. While the cell size is not explicitly adjusted in the proposed model, we can instead achieve a similar result by prescribing a wide gas temperature distribution. This is because a fire (or hot gas) approaching a larger cell results in a wide range of sub-grid temperatures given only the temperature of a small fraction of the large cell would initially increase while the remainder of the cell remains closer to the ambient temperature. In the next phases of this work, the inclusion of advection and turbulent diffusion, as well as influences on local gas temperature distributions are incorporated to account for cell size effects. These will feed back to the solid phase equations presented here. However, we can explore this concept by modifying the prescribed gas temperature distribution shown in Figure 17. In these simulations, we assign a mean gas temperature of 500 K in the control volume and apply a range of variances for the moisture fraction 1 scenario under all 3 wind speed cases. The value indicated by x in ϕ_{gx} represents half the width of the top hat distribution, i.e., 500 + ϕ_{gx} K is the maximum temperature in the top hat distribution with ϕ_{gx} ranging from 100 to 300 K. This Figure highlights that increasing width of the gas temperature distribution results in an increase in width of the fuel temperature distribution in all wind cases, regardless of the state of combustion. Furthermore, increasing the wind speed (and thus convective heat transfer) increases dry fuel temperature variance in both combustion and non-combustion scenarios. This is because stronger convection will result in a stronger influence of the gas temperature on solid temperature.

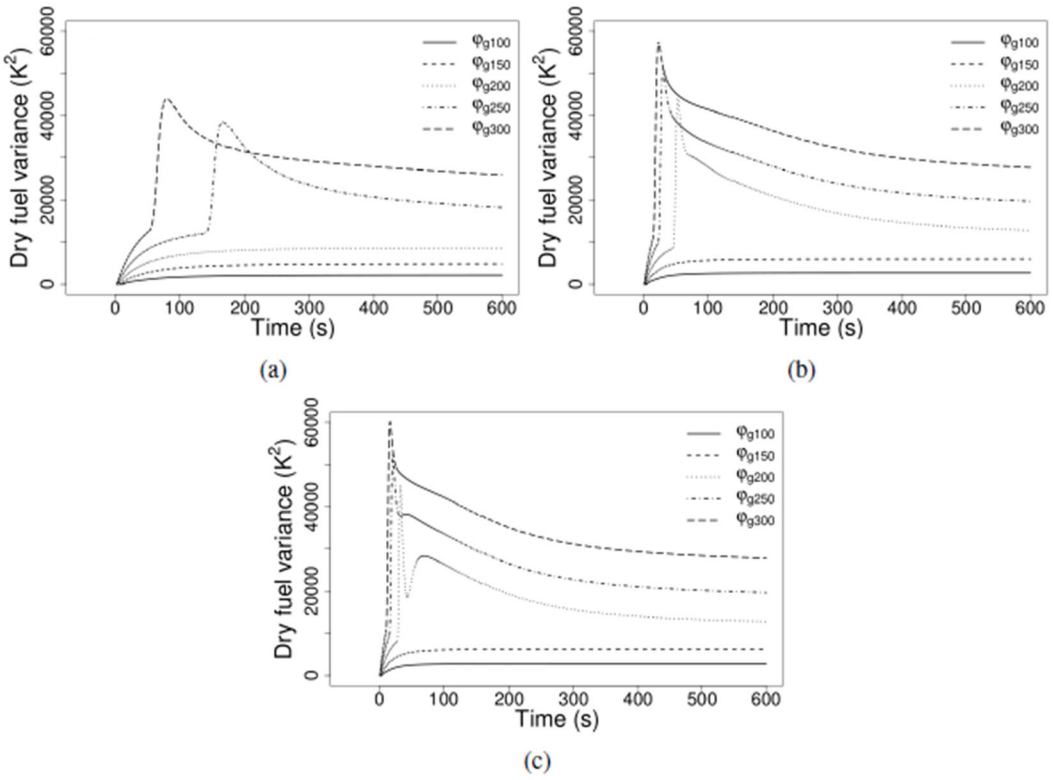

Figure 17: Comparison of the effects for different gas temperature variances on the dry fuel variance for a) 0.1 m s^{-1}, b) 1.0 m s^{-1} and c) 2.0 m s^{-1} winds. In all simulations the mean gas temperature is 500 K, the moisture fraction is 1 and ϕ_{gx} is a measure of the gas temperature variance, with x corresponding to half the maximum width of the top hat.

Currently, FIRETEC simulations require significant computational resources on high-performance computing systems due in part to restrictions on grid spacing. A single simulation in a small domain (e.g., 200 cells x 200 cells x 41 cells) requires tracking over 1.6 million cells, and within each of those cells computing or storing upwards of 40 variables at each time step with time steps as small as 0.001s. Increasing the cell size has the potential to reduce computing requirements without compromising modeled fire behavior and will be examined in future work.

Field Experiments and Model Comparison

On the afternoon of November 15, 2017 a series of experimental fires were conducted between 1700 and 1800 UTC, providing data for the evaluation of the overall performance of the proposed model. For these experiments, a 4x4 m sand bed was constructed on the campus of the University of Georgia, Athens, GA and a 2:4 2:4 m burn area was established inside the sand bed. Further details on the experimental fire bed configuration can be found in Strother (2020). The fuel bed consisted of pine litter with a 4% moisture content, which was spread across the burn area to

achieve a fuel load of 0.37 kg m^{-2} approximately 10 cm deep. The weather station located on Whitehall Forest recorded mean wind speeds of 0.635 and 0.474 m s^{-1} for the hours of 1700 and 1800 UTC respectively with the maximum gust of 1:21 m s^{-1}. The imaging system consisted of a FLIR (Forward Looking Infrared) SC660 (FLIR Systems Inc., Boston, MA, USA) thermal imaging system mounted to a 7 m-tall aluminum tripod which was positioned directly above the burn area to provide a nadir view. The FLIR system has a focal plane array of 640 480 pixels and a spatial resolution of 0:9 cm at 7 m distance. The temperature range selected for data collection during the fires was 573 to 1773 K at a measurement rate of 1 Hz. Further details on FLIR specifications are found elsewhere (e.g., Hiers et al. 2009; Loudermilk et al. 2012; O'Brien et al. 2016). Visual imagery was captured by a GoPRO HERO3 camera mounted alongside the FLIR. Three different ignition patterns were completed: a point source, ring source, and 2 parallel lines. Four 1 1 m cells were segregated for each experimental fire and temperature distributions within each cell were analyzed at each second.

Precise descriptions of the gas temperature and associated variance are unknown for these experiments. Given the lower intensity of the fire, we approximate the upwind gas temperature as

$$\bar{T}_{g_{uw}} = 300 + 500\tanh\left(\frac{t-30}{100}\right) + 400\tanh\left(\frac{400-t}{1000}\right), \tag{63}$$

which allows for a slow gas temperature rise. The gas temperature variance, like the idealized scenarios previously discussed, is assigned to have a variance

$$\overline{T_g' T_g'} = \left(60 + \frac{\bar{T}_g - 300}{6}\right)^2. \tag{64}$$

Fuel bed temperature is initialized at 292 K and we estimate the ground level winds and TKE as U = 0:4 m s^{-1}, k_a = 0:05 m s^{-1}, and k_b = 0:002 m s^{-1} (used for the mixing limited reaction rate) near the ground.

The completed simulation compared to the observations is illustrated in Figure 18, where the dashed lines are the mean temperatures of the various burning observations within the 1x1m cell, the red solid line with squares indicates modeled mean dry temperature, the blue solid line with circles is mean wet fuel temperature, the grey line is gas temperature and shading indicates one standard deviation above and below the mean based on the dry and wet modeled variances. The observed data is only presented for values above 773 K. Since there are multiple fire observations, we align the model data with the observations at peak temperatures. Furthermore, it is important to note that FLIR temperature observations are from the two-dimensional surface layer and do not capture variations in temperature below the surface. The proposed model, however, accounts for three-dimensional temperature distributions. With that said, unsurprisingly, the observed fuel temperatures are significantly hotter than the modeled mean temperatures. However, if we truncate the simulation data (from the modeled mean temperature and variance) to values in the distribution greater than 773 K, we observe a

significant improvement in the alignment between modeled and observed temperature, especially after the peak temperature as shown by the solid black line. Distinct differences include a more rapid modeled rise in temperature during the initial combustion phase with a slightly premature drop in temperature as fuel is being consumed and a slower reaction rate. As previously discussed in the idealized scenarios, we hold the upwind gas temperature constant. Thus, we are not capturing the turbulent gas temperature variations that would influence fire behavior. These limitations are not associated with the final model, but instead are the result of the overly simplified test cases presented here.

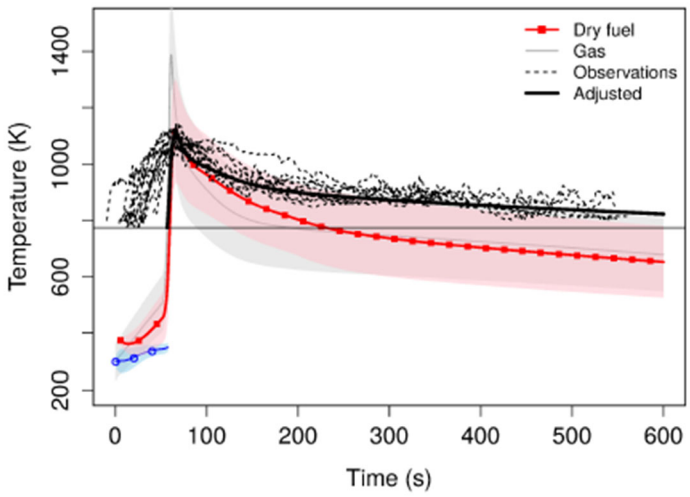

Figure 18: Simulation results for the mean wet solid fuel, dry fuel and gas temperatures (blue, red,grey solid lines) compared with observations (dashed lines) of mean solid temperature evolution in a 1 m x 1 m cell. The horizontal line is at 773 K (500 C) which is the minimum observed FLIR temperature. The adjusted dry fuel temperature (thick solid black line) is the recalculated mean temperature for temperatures above 773 K.

Figure 19 illustrates the modeled variance and the observed variance. In this figure, the red solid line with squares is the modeled variance, the light grey line is the prescribed gas temperature variance and the dashed lines indicate the ensemble of mean variance observations. While the observed variances are approximately half to three-quarters of the modeled values (in red), this is not necessarily a case of overestimation by the modeled variance. Rather, it is the result of a restricted range of observed temperatures measured by the FLIR. It is reasonable to assume that temperatures within a single cell solid would be below 500 C during a low intensity fire, which is not accounted for in these observations. Thus, the results show fictitiously low variance. Furthermore, the three-dimensional distribution of temperatures, which are not accounted for in the FLIR observations, would further increase the variance. This is because deeper fuel initially

has lower temperatures compared to the surface temperature, which would be exposed to convective and radiant heating ahead of the flame front. As discussed in the previous figure with a mean temperature adjustment, we similarly observe a more realistic modeled variance by excluding fuels below 773 K. While the magnitude of the modeled variance does not reflect the observed variance presented here, the overall shape and behavior of the variance aligns with the shape and behavior of the observed variance. Given the strong influence of the gas temperature variance on the fuel temperature variance, improvements to modeled gas temperature will improve the overall model performance.

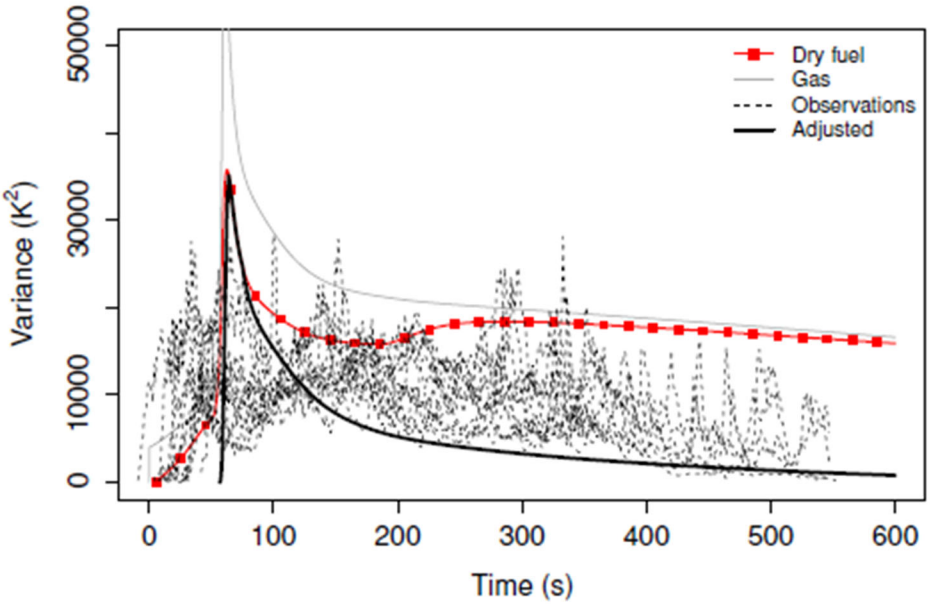

Figure 19: Simulation results for modeled variance (solid line) compared with observations of variance in a 1 m x 1 m cell. The adjusted variance is recalculated after removing all temperatures below 773 K, as discussed in Figure 18.

Conclusions and future work

A new parameterization for sub-grid processes related to temperature and moisture variation in wildfire behavior models has been developed. Other wildfire behavior models have succeeded in simulating high-intensity fire during extreme conditions where the relevant length scales are large enough to be resolved and the impact of sub-grid variations is minimal. However, the performance of these models suffers when conditions are less extreme and the length scales are small. The aim of the work described here is to improve the overall performance of these models, particularly during lower-intensity fires where the sub-grid spatial and temporal variations have significant impacts on fire behavior.

The focus of this project was improving the parameterization of the combustion process in coupled fire-atmosphere models by better describing the governing equations for wet and dry fuels and their temperature evolution. Our future plan (currently ongoing) is to focus on the development of equations describing the evolution of the temperature variations for the gas phase based on a similar approach as described here. These new equations for the gas phase will then be coupled to the set of equations for the wet and dry fuels, which should improve the modeled energy exchange between wet and dry fuel and surrounding gas. This has a significant influence on fire behavior as we have previously shown. This energy exchange is one of the essential components contributing to the self-determining nature of FIRETEC. As such, considerable effort is being put toward these next developments.

References

Accary, G., Meradji, S., Morvan, D., Bessonov, O. & Fougere, D. 2014 FireStar3D: 3D finite volume model for the prediction of wildfires behaviour, pp. 251–260. Coimbra: Imprensa da Universidade de Coimbra.

Besnard, Didier, Harlow, Francis H., Rauenzahn, Rick M. & Zemach, Charles 1992 Turbulence transport equations for variable-density turbulence and their relationship to two-field models. Tech. Rep.. Los Alamos National Laboratory.

Caccamo G, Chisholm LA, Bradstock RA, Puotinen ML (2012) Using remotely-sensed fuel connectivity patterns as a tool for fire danger monitoring. Geophysical Research Letters, 39 (L01302): 1-5.

Call, PT & Albini, FA 1997 Aerial and Surface Fuel Consumption in Crown Fires. International Journal of Wildland Fire 7 (3), 259–264.

Clements CB, Zhong S, Goodrick S, Li Ju, Potter BE, Bian X, Heilman WE, Charney JJ, Perna R, Jang M, Lee D, Patel M, Street S, Aumann G (2007) Observing The Dynamics Of Wildland Grass Fires: FireFlux -A Field Validation Experiment. Bulletin of the American Meteorological Society. 88(9):1369-1382.

Cheney, Phil & Sullivan, Andrew 2008 Grassfires : Fuel, Weather and Fire Behaviour, 2nd edn. Collingwood, VIC: CSIRO PUBLISHING.

Cohen, Jack & Finney, Mark 2022a Fuel particle heat transfer part 2: Radiation and convection during spreading laboratory fires. Combustion Science and Technology 0 (0), 1–26, arXiv: https://doi.org/10.1080/00102202.2021.2019232.

Cohen, Jack D. & Finney, Mark A. 2022b Fuel particle heat transfer part 1: Convective cooling of irradiated fuel particles. Combustion Science and Technology 0 (0), 1–27, arXiv: https://doi.org/10.1080/00102202.2021.2019231.

Daly, Bart J & Harlow, Francis H 1970 Transport equations in turbulence. The physics of fluids 13 (11), 2634–2649.

Drysdale, Dougal 1985 An introduction to fire dynamics. Tech. Rep.. Department of Fire Safety Engineering at University of Edinburgh.

Finney, Mark A., Cohen, Jack D., Forthofer, Jason M., McAllister, Sara S., Gollner, Michael J., Gorham, Daniel J., Saito, Kozo, Akafuah, Nelson K., Adam, Brittany A., English, Justin D. & Dickinson, Robert E. 2015 Role of buoyant flame dynamics in wildfire spread. Proceedings of the National Academy of Sciences of the United States of America 112 (32), 9833–9838.

Fleet D, Weiss Y (2006) Optical flow estimation. In Handbook of Mathematical Models in Computer Vision. Springer U.S. pp. 237-257.

Forestry Canada Fire Danger Group 1992 Development and Structure of the Canadian Forest Fire Behavior Prediction System. Tech. Rep.. Ottawa.

Freeborn PH, Wooster MJ, Hao WM, Ryan CA, Nordgren BL, Baker SP, Ichoku C (2008) Relationships between energy release, fuel mass loss, and trace gas and aerosol emissions during laboratory biomass fires Journal of Geophysical Research: Atmospheres (1984-2012), 113 (D1).

Giglioli N, Saltelli A (2011). Simlab - Software package for uncertainty and sensitivity analysis. Ispra, Italy: Institute for Systems Informatics and Safety (Joint Research Centre, European Commission).

de Groot, William J., Hanes, Chelene C. & Wang, Yonghe 2022 Crown fuel consumption in Canadian boreal forest fires. International Journal of Wildland Fire.

Hardy C, Heilman W, Weise D, Goodrick S, Ottmar R (2008) Final Report: Fire behavior advancement plan; a plan for addressing physical fire processes within the core fire science portfolio. 08-S-01 (Joint Fire Science Program).

Hiers, J. Kevin, O'Brien, Joseph J., Mitchell, R. J., Grego, John M. & Loudermilk, E. Louise 2009. The wildland fuel cell concept: an approach to characterize fine-scale variation in fuels and fire in frequently burned longleaf pine forests. International Journal of Wildland Fire 18 (3), 315–325.

Hoffman, C. M., Canfield, J., Linn, R. R., Mell,W., Sieg, C. H., Pimont, F.&Ziegler, J. 2016 Evaluating Crown Fire Rate of Spread Predictions from Physics-Based Models. Fire Technology 52 (1), 221–237.

Incropera, Frank P. & DeWitt, David P. 1996 Fundamentals of Heat and Mass Transfer, 4th edn. New York City, New York: John Wiley & Sons Inc.

Jolly, W. Matt, Hadlow, Ann M. & Huguet, Kathleen 2014 De-coupling seasonal changes in water content and dry matter to predict live conifer foliar moisture content. International Journal of Wildland Fire 23 (4), 480–489.

Jonko, Alexandra K., Yedinak, Kara M., Conley, Juliana L. & Linn, Rodman R. 2021 Sensitivity of grass fires burning in marginal conditions to atmospheric turbulence. Journal of Geophysical Research: Atmospheres 126 (13), e2020JD033384, arXiv: https://agupubs.onlinelibrary.wiley.com/doi/pdf/10.1029/2020JD033384.

Linn, Rodman 1997 A Transport Model for Prediction of Wildfire Behavior .

Linn, Rodman, Reisner, Jon, Colman, Jonah J. & Winterkamp, Judith 2002 Studying wildfire behavior using FIRETEC. International Journal of Wildland Fire 11 (4), 233–246.

Linn, R. R. & Cunningham, P. 2005 Numerical simulations of grass fires using a coupled atmosphere fire model: Basic fire behavior and dependence on wind speed. Journal of Geophysical Research Atmospheres 110 (13)

Linn, Rodman R., Winterkamp, Judith L., Furman, James H., Williams, Brett, Hiers, J. Kevin, Jonko, Alexandra, OaAZBrien, Joseph J., Yedinak, Kara M. & Goodrick, Scott 2021 Modeling Low Intensity Fires: Lessons Learned from 2012 RxCADRE. Atmosphere 12 (2).

Loudermilk EL, O'Brien JJ, Mitchell RJ, Hiers JK, Cropper Jr. WP, Grunwald S, Grego J, Fernandez J (2012). Linking complex forest fuel structure and fire behavior at fine scales. International Journal of Wildland Fire. 21:882-893

McNider RT, Song AJ, Casey DM, Wetzel PJ, Crosson WL, Rabin RM (1994) Toward a dynamic-thermodynamic assimilation of satellite surface temperature in numerical atmospheric models. Monthly Weather Review. 122: 2784-2803.

Mell, William, Jenkins, Mary Anne, Gould, Jim & Cheney, Phil 2007 A Phyics-Based Approach to Modelling Grassland Fires. International Journal of Wildland Fire 16, 1–22.

Mell, William, Maranghides, Alexander, McDermott, Randall & Manzello, Samuel L. 2009 Numerical Simulation and Experiments of Burning Douglas Fir Trees. Combustion and Flame 156 (10), 2023–2041.

Ng WB, Zhang Y (2005). Stereoscopic imaging and computer vision of impinging fires by a single camera with a stereo adapter. International Journal of Imaging Systems and Technology 15: 114–122.

O'Brien, Joseph J., Loudermilk, E. Louise, Hornsby, Benjamin, Hudak, Andrew T., Bright, Benjamin C., Dickinson, Matthew B., Hiers, J. Kevin, Teske, Casey & Ottmar, Roger D. 2016 High-resolution infrared thermography for capturing wildland fire behaviour: RxCADRE 2012. International Journal of Wildland Fire 25 (1), 62–75.

Parsons, Russell A., Mell, William E. & McCauley, Peter 2011 Linking 3d spatial models of fuels and fire: Effects of spatial heterogeneity on fire behavior. Ecological Modelling 222 (3), 679–691.

Prasad AK (2000). Stereoscopic particle image velocimetry. Experiments in Fluids. 29: 103-116.

Quenot GM, Pakleza J, Kowalewski TA (1998) Particle image velocimetry using optical flow for image analysis. 8th International Symposium on Flow Visualization.

Stocks, B. J., Alexander, M. E., Wotton, B. M., Stefner, C. N., Flannigan, M. D., Taylor, S. W., Lavoie, N., Mason, J. A., Hartley, G. R., Maffey, M. E., Dalrymple, G. N., Blake, T.W., Cruz, M. G. & Lanoville, R. A. 2004 Crown fire behaviour in a northern jack pine - Black spruce forest. Canadian Journal of Forest Research 34 (8), 1548–1560.

Strother, Dexter 2020 The role of black carbon in a longleaf pine ecosystem. PhD thesis, University of Georgia.

Taylor, S.W.,Wotton, B. M., Alexander, M. E. & Dalrymple, G. N. 2004 Variation in wind and crown fire behaviour in a northern jack pine - Black spruce forest. Canadian Journal of Forest Research 34 (8), 1561–1576.

Thompson, Dan K., Schroeder, Dave, Wilkinson, Sophie L., Barber, Quinn, Baxter, Greg, Cameron, Hilary, Hsieh, Rex, Marshall, Ginny, Moore, Brett, Refai, Razim, Rodell, Chris, Schiks, Tom, Verkaik, Gregory J. & Zerb, Jessica 2020 Recent Crown Thinning in a Boreal Black Spruce Forest Does Not Reduce Spread Rate nor Total Fuel Consumption: Results from an Experimental Crown Fire in Alberta, Canada. Fire 3 (3).

van der Kamp, D.W., Moore, R.D. & McKendry, I.G. 2017 A model for simulating the moisture content of standardized fuel sticks of various sizes. Agricultural and Forest Meteorology 236, 123–134.

Van Wagner CE (1968) The line intersect method in forest fuel sampling. Forest Science 14, 20

Wooster MJ (2002) Small-scale experimental testing of fire radiative energy for quantifying mass combusted in natural vegetation fires. Geophysical Research Letters. 29(21): 23-1.

Wooster MJ, Perry G, Zhukov B, Oertel D (2004) Biomass burning emissions inventories: Modelling and remote sensing of fire intensity and biomass combustion rates, in Spatial Modelling of the Terrestrial Environment, edited by Kelly R, Drake N, Barr S, John Wiley, Hoboken, NJ. pp. 175 – 196.

Wooster MJ, Roberts G, Perry GLW, Kaufman YJ (2005) Retrieval of biomass combustion rates and totals from fire radiative power observations: FRP derivation and calibration relationships between biomass consumption and fire radiative energy release. Journal of Geophysical Research: Atmospheres (1984-2012) 110 (D24)

Wotton, B. Mike, Gould, James S., McCaw, W. Lachlan, Cheney, N. Phillip & Taylor, Stephen W. 2012 Flame temperature and residence time of fires in dry eucalypt forest. International Journal of Wildland Fire 21 (3), 270–281.

Zhou, Xiangyang, Mahalingam, Shankar & Weise, David 2005 Modeling of marginal burning state of fire spread in live chaparral shrub fuel bed. Combustion and Flame 143 (3), 183–198.